

# Cooperative Transport via Flexible Cable Suspensions: Decentralized Geometric Control with Adaptive Estimation and Safety Guarantees

Hadi Hajieghrary<sup>1</sup>, Benedikt Walter<sup>2</sup>, Miguel Hurtado<sup>3</sup>, and Paul Schmitt<sup>4</sup>

**Abstract**—We present the Geometric Position and Attitude Control (GPAC) architecture for decentralized cooperative aerial transport via flexible cable suspensions. Each of  $N$  quadrotors operates with zero knowledge of the team size  $N$ , payload mass  $m_L$ , or any other agent’s state, yet the closed-loop system maintains geometric control on the full  $\text{SE}(3) \times (\mathbb{S}^2)^N$  configuration manifold with Lyapunov-certifiable stability guarantees. A concurrent learning adaptive law enables each drone to independently estimate its payload share  $\hat{\theta}_i \rightarrow m_L/N$  without persistent excitation, and a modular Control Barrier Function safety filter enforces cable tautness, swing angle, tilt, and collision constraints with input-to-state safety (ISSf) guarantees—bounding constraint violations under disturbances—provably compatible with the geometric attitude controller. The framework is validated in a high-fidelity Drake-based simulation incorporating flexible bead-chain cable dynamics, onboard sensor models (IMU, GPS, barometer) with Error-State Kalman Filter fusion, and Dryden wind turbulence. The decentralized architecture achieves 22.9 cm payload tracking RMSE, maintains safety constraints within ISSf margins, and requires less than 1 MFLOP/s per agent, demonstrating feasibility for embedded deployment.

## I. INTRODUCTION

Cooperative aerial transport—in which multiple unmanned aerial vehicles (UAVs) jointly manipulate a common payload via cable suspensions—has emerged as a compelling paradigm for extending the payload capacity, workspace, and fault tolerance of rotorcraft beyond the limits of any single platform. Applications range from construction logistics and emergency supply delivery to the assembly of large-scale structures in environments inaccessible to ground vehicles. The fundamental appeal is clear:  $N$  quadcopters, each rated for a maximum thrust  $T_i^{\max}$ , can collectively transport payloads approaching  $N$  times the capacity of an individual agent, while the spatial distribution of attachment points affords controllability over the payload’s full six-degree-of-freedom pose. Yet realizing this potential in practice demands controllers that are simultaneously *geometrically rigorous*—respecting the nonlinear manifold structure of the configuration space—and *operationally decentralized*, requiring neither a central coordinator nor inter-agent communication during flight.

The geometric mechanics of cable-suspended transport have been studied extensively since the seminal work of Lee, Sreenath, and Kumar [1], [2], who formulated the coupled dynamics of a quadrotor-load system on the configuration manifold  $\text{SE}(3) \times (\mathbb{S}^2)^N$  and derived controllers

with provable almost-global asymptotic stability guarantees. In this framework, the attitude of each quadrotor  $i$  evolves on the special orthogonal group  $\text{SO}(3)$ , while the cable direction  $q_i \in \mathbb{S}^2$  is a unit vector constrained to the two-sphere. The coupling between translational load dynamics and rotational cable swing is captured through the tangent-space projection  $P(q) = I_{3 \times 3} - qq^\top$  (9), and the attitude tracking error  $e_R$  (18) is defined directly on  $\text{SO}(3)$  via the vee map  $(\cdot)^\vee : \mathfrak{so}(3) \rightarrow \mathbb{R}^3$ , avoiding the singularities and unwinding phenomena inherent in Euler-angle or quaternion-based parameterizations. Subsequent extensions incorporated load swing suppression on  $\mathbb{S}^2$  using the configuration error function  $\Psi_q = 1 - q_d \cdot q$  (19) and the cable direction error  $e_q = P(q) q_d$  (20), together with geometric feedforward/feedback policies that yield exponential convergence of the cable direction to the desired equilibrium [3], [4]. These results constitute the theoretical gold standard for cable-suspended aerial manipulation.

However, many Lyapunov-certified geometric cooperative transport controllers assume centralized state knowledge. Each quadrotor’s control law requires global knowledge of the total number of agents  $N$ , the payload mass  $m_L$ , the full system state—including the states of all other agents—and often the complete allocation of desired forces across the team. These assumptions permit elegant closed-form stability proofs but render the resulting controllers impractical for deployment. In realistic multi-agent scenarios, the team size  $N$  may change due to agent failures or additions, the payload mass  $m_L$  is typically uncertain, and reliable high-bandwidth inter-agent communication cannot be guaranteed. The gap between the mathematical elegance of geometric cooperative transport theory and the operational requirements of decentralized deployment remains largely unaddressed.

Conversely, the adaptive and decentralized multi-robot control literature addresses many of these practical constraints but typically at the cost of geometric fidelity. Consensus-based formation controllers [5], distributed optimization methods, and adaptive impedance strategies have been proposed for cooperative manipulation tasks, but these approaches predominantly rely on linearized dynamics, Euclidean error metrics, and small-angle approximations that forfeit the global stability guarantees and singularity-free operation that geometric methods provide. In particular, linearized attitude representations break down during the large-angle maneuvers that commonly arise during payload pickup, aggressive trajectory tracking, and disturbance recovery—

<sup>1</sup>Hadi Hajieghrary {Hadi.Hajieghrary@gatech.edu}, ...

precisely the operating regimes where formal stability guarantees are most needed. Meanwhile, adaptive estimation techniques for uncertain parameters, such as model reference adaptive control (MRAC) and composite adaptation, have been developed for single-vehicle systems but have not been integrated with the coupled geometric dynamics of multi-agent cable-suspended transport. The concurrent learning paradigm [6], [7], which enables parameter convergence without persistent excitation (PE) by exploiting stored data, is particularly relevant for cooperative transport where the nominal hover condition provides limited excitation; yet existing applications remain confined to centralized single-vehicle settings.

A parallel challenge concerns safety-critical operation. Cable-suspended transport imposes multiple state constraints that must be enforced in real time: cables must remain taut to maintain controllability, cable angles must stay within bounds to prevent entanglement and load instability, swing rates must be limited to avoid resonant excitation, and inter-agent collisions must be prevented. Control Barrier Functions (CBFs) [8], [9] have emerged as a principled framework for enforcing such constraints via online quadratic program (QP) filters that minimally modify a nominal controller to guarantee forward invariance of a safe set. However, integrating CBF-based safety filters with geometric controllers on nonlinear manifolds—while preserving the underlying Lyapunov stability certificates—remains challenging, particularly in the decentralized multi-agent setting where coupled constraints and attitude stability certificates must coexist.

Furthermore, the majority of existing geometric transport analyses assume idealized cable models—either rigid links or massless inextensible strings—that cannot capture the rich dynamics of real flexible cables. In practice, cables exhibit compliance, wave propagation, slack-to-taut transitions, and distributed inertia effects that significantly influence the coupled system behavior. These phenomena are especially pronounced during the critical payload pickup phase, where ropes transition from slack to taut and impulsive forces can destabilize the formation. Bead-chain discretizations, in which the cable is modeled as a series of point masses connected by tension-only spring-damper elements, provide a physically faithful representation of these effects [10], but their integration with geometric controllers has received limited attention.

Finally, the vast majority of geometric control results for cooperative transport are validated under the assumption of perfect state feedback. In practice, onboard state estimation must fuse noisy, heterogeneous sensor measurements—*inertial measurement units (IMUs)* subject to Gauss-Markov bias drift, GPS receivers with intermittent dropouts, and barometric altimeters with correlated noise—through nonlinear filtering pipelines such as the Error-State Kalman Filter (ESKF) [11]. Wind disturbances, modeled here via the Dryden turbulence spectrum [12], introduce additional unmodeled forces that must be rejected. The robustness of geometric cooperative transport controllers to realistic estimation errors and environmental disturbances remains

largely uncharacterized.

This paper presents a unified framework that bridges these two bodies of literature—geometric control theory and decentralized adaptive systems—in a unified framework for cooperative cable-suspended aerial transport. We propose the **Geometric Position and Attitude Control (GPAC)** architecture: a four-layer hierarchical controller in which each quadrotor operates with *zero knowledge* of the total agent count  $N$ , the payload mass  $m_L$ , or any other agent's state, yet the closed-loop system maintains geometric control on the full  $\text{SE}(3) \times \mathbb{S}^2$  configuration manifold with Lyapunov-certifiable convergence guarantees. The architecture is validated in a high-fidelity Drake-based simulation environment incorporating flexible bead-chain cable dynamics, realistic onboard sensors, and Dryden wind turbulence.

The specific contributions of this work are as follows. At the highest level, the GPAC architecture decomposes the cooperative transport problem into  $N$  identical single-agent subproblems. Each drone independently estimates only its own share of the payload mass,  $\hat{\theta}_i \approx m_L/N$ , using local cable tension and direction measurements. The key insight is that when all agents do this simultaneously, their combined forces automatically sum to the correct total—no explicit coordination required. A modular safety filter overlays the resulting controller to enforce physical constraints (cable tautness, collision avoidance) with minimal performance impact.

- 1) **Decentralized geometric cooperative transport with formal stability guarantees.** We derive an operationally decentralized control law—no peer-to-peer state exchange is required at runtime; each agent receives only the shared reference trajectory via a common broadcast—in which each quadrotor's policy depends only on its own state and local cable-tension and direction measurements. No drone requires knowledge of  $N$  or  $m_L$ . The control is formulated directly on  $\text{SO}(3) \times \mathbb{S}^2$  using the attitude error (18) and the  $\mathbb{S}^2$  cable direction error (20), preserving global geometric structure. Unlike prior decentralized controllers that linearize around hover or use Euclidean error metrics, this is, to our knowledge, the first decentralized geometric controller for multi-UAV cable transport that operates directly on the nonlinear  $\text{SE}(3) \times (\mathbb{S}^2)^N$  manifold. The key theoretical novelty is proving that independent local estimation of  $\hat{\theta}_i$  yields implicit coordination (1) without requiring any communication or parameter sharing—a property that does not hold for linearized or impedance-based decentralized approaches. We show that when each agent independently estimates its load share parameter  $\hat{\theta}_i \rightarrow m_L/N$ , the summed forces automatically converge to the correct total without explicit coordination:

$$\sum_{i=1}^N F_i = \sum_{i=1}^N \hat{\theta}_i \cdot u \longrightarrow m_L \cdot u. \quad (1)$$

- 2) **Concurrent learning adaptive estimation without persistent excitation.** We introduce a decentralized

adaptive estimation scheme in which each drone independently estimates the ratio  $\hat{\theta} = m_L/N$  using only its local cable tension  $T_i$ , cable angle  $\phi_i$ , and load acceleration estimate. The key insight is that

$$\frac{T_i \cos \phi_i}{\|g e_3 + a_L\|} \rightarrow \frac{m_L}{N}, \quad (2)$$

the quantity each drone actually needs, without requiring knowledge of either  $m_L$  or  $N$  individually. A concurrent learning algorithm [6] with a rank-maximizing history stack of regressor–output pairs  $(Y_j, z_j)$  ensures parameter convergence via the update law

$$\dot{\hat{\theta}} = \Gamma \left( Y^\top s + \rho \sum_{j=1}^M Y_j^\top (Y_j \hat{\theta} - z_j) \right), \quad (3)$$

without the persistent excitation condition—which is critical because cooperative hover, the nominal operating condition, provides insufficient excitation for classical adaptive laws. The theoretical contribution is the adaptation of concurrent learning to a decentralized multi-agent geometric setting, where each agent’s regressor is constructed from purely local cable measurements. This is non-trivial because the regressor vector depends on the coupled system dynamics, yet we show that the local tension equilibrium (2) provides a sufficient scalar parametric model for each agent independently.

- 3) **Multi-rate hierarchical architecture with time-scale separation.** The GPAC architecture implements a four-layer cascade with deliberate bandwidth separation:

- *Layer 1 ( $\sim 50\text{Hz}$  effective):* Position tracking with  $\mathbb{S}^2$  anti-swing control, producing a desired thrust direction from the force command

$$F_{\text{des}} = -K_p(p-p_d) - K_d(\dot{p}-\dot{p}_d) + \hat{\theta}(g e_3 + \ddot{p}_d^L) + F_{\text{swing}}, \quad (4)$$

where  $F_{\text{swing}} = k_q e_q + k_\omega(q_d \times \omega_q)$  damps cable oscillations on the tangent space  $T_q \mathbb{S}^2$ .

- *Layer 2 (200Hz):* Geometric SO(3) attitude tracking with the control torque

$$\tau = -K_R e_R - K_\Omega e_\Omega + \Omega \times J \Omega + J(\hat{\Omega} R^\top R_d \Omega_d - R^\top R_d \dot{\Omega}_d) - \hat{d}, \quad (5)$$

where  $e_\Omega = \Omega - R^\top R_d \Omega_d$  is the angular velocity error and  $\hat{d}$  is the ESO disturbance estimate.

- *Layer 3 (50Hz):* Concurrent learning parameter estimation via (3).
- *Layer 4 (continuous,  $\omega_0 = 50\text{ rad/s}$ ):* Third-order Extended State Observer (ESO) per translational axis,

$$\dot{\hat{x}}_1 = \hat{x}_2 + 3\omega_0 \tilde{x}, \quad \dot{\hat{x}}_2 = \hat{x}_3 + 3\omega_0^2 \tilde{x}, \quad \dot{\hat{x}}_3 = \omega_0^3 \tilde{x}, \quad (6)$$

with  $\tilde{x} = x - \hat{x}_1$  and bandwidth  $\omega_0 = 50\text{ rad/s}$ , estimating the lumped disturbance  $\hat{d} = \hat{x}_3$ .

The deliberate time-scale separation enables independent Lyapunov analysis of each layer while the cascade composition preserves overall closed-loop stability, making the decentralized stability proof tractable via

singular perturbation arguments.

- 4) **Modular CBF safety filter preserving geometric stability certificates.** We design a Control Barrier Function safety layer implemented as an online QP that bounds safety constraint violations via ISSf margins. Defining barrier functions for cable tautness  $h_1 = \|p_q - p_L\| - L_{\min}$ , cable angle  $h_2 = \cos \theta - \cos \theta_{\max}$ , swing rate bounds, vehicle tilt limits, and inter-agent collision avoidance, the safety filter solves

$$\min_{u, \delta} \|u - u_{\text{nom}}\|^2 + \lambda \delta^2 \quad \text{s.t. } \dot{h}_k + \alpha_k h_k \geq -\delta_k, \quad \forall k, \quad (7)$$

where  $u_{\text{nom}}$  is the geometric controller output,  $\alpha_k > 0$  are class- $\mathcal{K}$  coefficients, and the slack variables  $\delta_k$  resolve potential conflicts between competing constraints and the geometric controller’s convergence requirements. Higher-order CBF (HOCBF) formulations handle relative-degree-two constraints, such as cable tautness, and a second-order Butterworth filter provides smooth tension-rate estimates for the constraint Jacobians. The filter operates as a modular overlay, minimally modifying the nominal geometric control input to enforce constraint satisfaction. The key theoretical result (Theorem 5.4) establishes that the CBF safety filter preserves the almost-global exponential stability certificate of the geometric attitude controller—a compatibility proof that requires bounding the attitude perturbation induced by the force modification on  $\text{SO}(3)$ . This compatibility argument, specific to the cable-transport setting, shows that the CBF-induced attitude perturbation remains within the almost-global stability region of the geometric controller under bounded disturbances and within the ISSf inflation  $\mathcal{C}_\mu$ .

- 5) **Sensor-realistic validation with flexible cable dynamics.** The complete framework is validated in a Drake-based [13] multibody simulation incorporating:

- a) Flexible cables modeled as bead-chain discretizations with  $n_b = 8$  point-mass beads per cable and  $n_b + 1 = 9$  tension-only spring-damper segments that naturally capture slack-to-taut transitions, wave propagation, and distributed inertia;
- b) A full onboard sensor suite comprising IMUs with Gauss–Markov bias dynamics (noise density  $\sigma_a = 0.004 \text{ m/s}^2/\sqrt{\text{Hz}}$ ,  $\sigma_g = 5 \times 10^{-4} \text{ rad/s}/\sqrt{\text{Hz}}$ , bias time constant  $\tau_b = 3600\text{s}$ ), GPS receivers with stochastic dropouts ( $\sigma_{xy} = 0.02 \text{ m}$ ,  $\sigma_z = 0.05 \text{ m}$ ), and barometric altimeters with correlated noise ( $\sigma_w = 0.3 \text{ m}$ , correlation time  $\tau_c = 5 \text{ s}$ , drift rate  $0.002 \text{ m/s}$ );
- c) A 15-state ESKF with error state  $\delta x = [\delta p, \delta v, \delta \theta, \delta b_a, \delta b_g]^\top \in \mathbb{R}^{15}$  fusing these heterogeneous measurements;
- d) Dryden-spectrum wind turbulence with turbulence intensities  $\sigma_u = \sigma_v = 0.5 \text{ m/s}$ ,  $\sigma_w = 0.25 \text{ m/s}$ , and altitude-dependent scaling.

This constitutes a high-fidelity simulation study incorporating flexible cable dynamics, multi-rate sensor mod-

els, and atmospheric turbulence, providing a rigorous validation environment for the proposed architecture.

Taken together, these contributions demonstrate that it is possible to simultaneously achieve operational decentralization, geometric rigor on the proper configuration manifold, ISSf safety guarantees bounding constraint violations under disturbances, and robustness to realistic sensing and environmental conditions—addressing the critical deployment gap that has prevented geometric cooperative transport theory from transitioning to operational multi-agent systems. The key enabling insight is the  $\hat{\theta} = m_L/N$  estimation architecture, which reduces the cooperative transport problem to  $N$  identical single-agent problems whose solutions automatically compose to the correct collective behavior without explicit coordination or parameter sharing.

The remainder of this paper is organized as follows. Section II formalizes the multi-body dynamic model on  $\text{SE}(3) \times (\mathbb{S}^2)^N$ , including the bead-chain cable model, sensor noise models, and wind disturbance characterization. Section III presents the GPAC hierarchical control architecture, deriving the control laws for each layer and establishing the individual and cascade stability properties. Section IV details the decentralized adaptive estimation scheme and its convergence guarantees under concurrent learning. Section V formulates the CBF safety filter and proves compatibility with the geometric controller. Section VI describes the Drake simulation environment, sensor models, and implementation details. Section VII presents comprehensive simulation results for multi-phase transport scenarios including hover, ascent, lateral translation, and descent under wind disturbance and sensor noise, with comparisons to centralized baselines and ablation studies. Section VIII concludes with a discussion of limitations and directions for future work, including experimental validation on physical platforms.

## II. SYSTEM MODELING

This section formalizes the multi-body dynamic model underlying the cooperative transport system. We begin with the individual quadrotor dynamics on  $\text{SE}(3)$ , then derive the coupled load–cable dynamics on  $\text{SE}(3) \times (\mathbb{S}^2)^N$ , present the flexible bead-chain cable discretization, and conclude with the sensor noise models and wind disturbance characterization that define the estimation environment.

### A. Notation and Geometric Preliminaries

We denote the world (inertial) frame by  $\mathcal{W}$  with orthonormal basis  $\{e_1, e_2, e_3\}$  and  $e_3$  aligned with the upward vertical. The special orthogonal group  $\text{SO}(3) = \{R \in \mathbb{R}^{3 \times 3} \mid R^\top R = I, \det(R) = 1\}$  represents the space of rotation matrices. Its Lie algebra  $\mathfrak{so}(3)$  is identified with the space of  $3 \times 3$  skew-symmetric matrices. The *hat map*  $(\cdot)^\wedge : \mathbb{R}^3 \rightarrow \mathfrak{so}(3)$  and its inverse, the *vee map*  $(\cdot)^\vee : \mathfrak{so}(3) \rightarrow \mathbb{R}^3$ , establish the isomorphism

$$\hat{v} = \begin{bmatrix} 0 & -v_3 & v_2 \\ v_3 & 0 & -v_1 \\ -v_2 & v_1 & 0 \end{bmatrix}, \quad \hat{v} w = v \times w, \quad \forall v, w \in \mathbb{R}^3. \quad (8)$$

TABLE I: Principal notation and symbols.

Symbol	Description
$\mathcal{W}$	World (inertial) frame
$\text{SO}(3)$	Special orthogonal group (rotations)
$\mathbb{S}^2$	Unit two-sphere (cable directions)
$\text{SE}(3)$	Special Euclidean group (rigid-body poses)
$P(q)$	Tangent-space projection on $\mathbb{S}^2$
$(\cdot)^\wedge, (\cdot)^\vee$	Hat map / vee map
$N$	Number of quadrotors
$m_Q, m_L$	Quadrotor mass, payload mass
$p_i, R_i, \Omega_i$	Position, rotation, angular velocity of drone $i$
$q_i \in \mathbb{S}^2$	Cable direction unit vector (payload $\rightarrow$ drone)
$T_i$	Cable tension magnitude
$e_{R_i}, e_{\Omega_i}$	Attitude and angular velocity errors on $\text{SO}(3)$
$\Psi_{q_i}, e_{q_i}$	Configuration and direction errors on $\mathbb{S}^2$
$\theta = m_L/N$	Per-drone payload mass share
$\hat{\theta}_i$	Adaptive estimate of $\theta$ by drone $i$
$\hat{d}_i$	ESO lumped disturbance estimate
$h_k$	Barrier function for safety constraint $k$
$\alpha_k$	Class- $\mathcal{K}$ CBF coefficient for constraint $k$

The unit two-sphere  $\mathbb{S}^2 = \{q \in \mathbb{R}^3 \mid \|q\| = 1\}$  represents the space of cable directions. The tangent space at  $q \in \mathbb{S}^2$  is  $T_q \mathbb{S}^2 = \{v \in \mathbb{R}^3 \mid q^\top v = 0\}$ , and the orthogonal projection onto  $T_q \mathbb{S}^2$  is

$$P(q) = I_{3 \times 3} - qq^\top. \quad (9)$$

The special Euclidean group  $\text{SE}(3) = \text{SO}(3) \ltimes \mathbb{R}^3$  is the configuration space of a rigid body with rotation  $R \in \text{SO}(3)$  and position  $p \in \mathbb{R}^3$ .

Table I summarizes the principal notation used throughout the paper.

### B. Quadrotor Dynamics on $\text{SE}(3)$

Consider  $N$  identical quadrotors, indexed by  $i \in \{1, \dots, N\}$ . Each quadrotor is modeled as a rigid body with mass  $m_Q$  and body-frame inertia tensor  $J \in \mathbb{R}^{3 \times 3}$ . Let  $p_i \in \mathbb{R}^3$  and  $R_i \in \text{SO}(3)$  denote the position and orientation of the  $i$ -th quadrotor's center of mass expressed in  $\mathcal{W}$ , and let  $\Omega_i \in \mathbb{R}^3$  denote its angular velocity in the body frame. The translational and rotational equations of motion are

$$m_Q \ddot{p}_i = m_Q g e_3 + f_i R_i e_3 + F_i^{\text{cable}} + F_i^{\text{wind}}, \quad (10)$$

$$J \dot{\Omega}_i = -\Omega_i \times J \Omega_i + \tau_i + \tau_i^{\text{ext}}, \quad (11)$$

where  $g = 9.81 \text{ m/s}^2$  is gravitational acceleration (acting downward; we adopt the convention  $e_3$  pointing up, so gravity is  $-g e_3$  in the world frame, with the control thrust  $f_i R_i e_3$  directed along the body  $z$ -axis),  $f_i \in \mathbb{R}$  is the scalar thrust magnitude,  $\tau_i \in \mathbb{R}^3$  is the control torque vector in the body frame,  $F_i^{\text{cable}} \in \mathbb{R}^3$  is the cable tension force at the attachment point, and  $F_i^{\text{wind}} \in \mathbb{R}^3$  is the aerodynamic disturbance. The kinematic relation between orientation and angular velocity is

$$\dot{R}_i = R_i \widehat{\Omega}_i. \quad (12)$$

Each quadrotor is parameterized with mass  $m_Q = 1.5 \text{ kg}$  and body dimensions  $0.30 \times 0.30 \times 0.10 \text{ m}$ , yielding a uniform-box inertia tensor.

### C. Payload Dynamics

The payload is modeled as a rigid body of mass  $m_L$  with center-of-mass position  $p_L \in \mathbb{R}^3$  and orientation  $R_L \in \text{SO}(3)$ . The  $N$  cable attachment points on the payload surface are located at fixed offsets  $\rho_i^L$  in the payload body

frame. In the simulation, the payload is a sphere of mass  $m_L = 3.0 \text{ kg}$  and radius  $r_L = 0.15 \text{ m}$ , resting on a ground plane with Coulomb friction (static coefficient  $\mu_s = 0.5$ , kinetic coefficient  $\mu_k = 0.3$ ). The translational dynamics are

$$m_L \ddot{p}_L = -m_L g e_3 + \sum_{i=1}^N F_i^L + F^{\text{contact}} + F_L^{\text{wind}}, \quad (13)$$

where  $F_i^L \in \mathbb{R}^3$  is the cable force from the  $i$ -th rope acting at the  $i$ -th attachment point on the payload,  $F^{\text{contact}}$  denotes the ground normal and friction forces, and  $F_L^{\text{wind}}$  is the wind disturbance on the payload.

#### D. Cable Direction and the Configuration Manifold

Under the assumption of taut, approximately inextensible cables, the direction from each quadrotor's attachment point to the payload attachment point defines a unit vector  $q_i \in \mathbb{S}^2$ . Letting  $L_i$  denote the effective cable length, the constraint

$$p_i + r_i^Q = p_L + R_L \rho_i^L + L_i q_i \quad (14)$$

relates the quadrotor and payload positions, where  $r_i^Q$  is the cable attachment offset in the quadrotor body frame and  $q_i$  points from the payload toward the quadrotor. The full configuration of the coupled system lies on the product manifold

$$\mathcal{Q} = \underbrace{\text{SE}(3)}_{\text{payload}} \times \prod_{i=1}^N \underbrace{\text{SE}(3) \times \mathbb{S}^2}_{\text{quadrotor } i}, \quad (15)$$

which has dimension  $6 + N \times 8 = 6 + 8N$  (6 for payload, 6 for each quadrotor's pose, and 2 for each cable direction on  $\mathbb{S}^2$ ).

The cable direction kinematics on  $\mathbb{S}^2$  are governed by

$$\dot{q}_i = \omega_{q_i} \times q_i, \quad \omega_{q_i} \in T_{q_i} \mathbb{S}^2, \quad (16)$$

where  $\omega_{q_i}$  is the angular velocity of the cable direction. On the tangent space, the swing dynamics are [3]

$$\ddot{q}_i = P(q_i) \left( \frac{1}{L_i} (u_{p_i} + u_{d_i}) - \frac{g}{L_i} (e_3^\top q_i) q_i \right) - \|\dot{q}_i\|^2 q_i, \quad (17)$$

where  $u_{p_i}$  and  $u_{d_i}$  are the proportional and derivative anti-swing control terms projected onto  $T_{q_i} \mathbb{S}^2$ .

The geometric error functions used for control on  $\text{SO}(3)$  and  $\mathbb{S}^2$  are the attitude error

$$e_{R_i} = \frac{1}{2} (R_{d_i}^\top R_i - R_i^\top R_{d_i})^\vee, \quad (18)$$

the configuration error on  $\mathbb{S}^2$

$$\Psi_{q_i} = 1 - q_{d_i} \cdot q_i \in [0, 2], \quad (19)$$

and the cable direction error

$$e_{q_i} = P(q_i) q_{d_i}. \quad (20)$$

Note that  $\Psi_{q_i} = 0$  if and only if  $q_i = q_{d_i}$  (perfect alignment), and  $\Psi_{q_i} = 2$  when  $q_i = -q_{d_i}$  (anti-aligned), while  $e_{q_i}$  is the negative gradient of  $\Psi_{q_i}$  restricted to  $T_{q_i} \mathbb{S}^2$  [1].

#### E. Flexible Cable Model: Bead-Chain Discretization

Rather than assuming rigid links or massless inextensible strings, we model each cable as a *bead-chain*: a series of  $n_b$  point-mass beads connected by  $n_b + 1$  tension-only spring-damper segments, as illustrated in Fig. ???. This discretization

captures the essential physics of flexible cables—compliance, wave propagation, slack-to-taut transitions, and distributed inertia—while remaining tractable for real-time simulation.

##### 1) Segment Force Law

Let  $b_0$  denote the quadrotor attachment point,  $b_1, \dots, b_{n_b}$  the bead positions, and  $b_{n_b+1}$  the payload attachment point. The  $j$ -th segment connects bodies  $b_{j-1}$  and  $b_j$  with rest length  $L_0 = L_{\text{rest}}/(n_b + 1)$ , where  $L_{\text{rest}}$  is the total rope rest length. The displacement vector, distance, and unit direction are

$$d_j = b_{j-1} - b_j, \quad \ell_j = \|d_j\|, \quad \hat{e}_j = d_j/\ell_j. \quad (21)$$

The stretch and stretch rate are

$$\Delta_j = \ell_j - L_0, \quad \dot{\Delta}_j = \hat{e}_j^\top (\dot{b}_{j-1} - \dot{b}_j). \quad (22)$$

The *tension-only* spring-damper force law is

$$T_j = \begin{cases} k_s \Delta_j + c_s [\dot{\Delta}_j]^+, & \text{if } \Delta_j > 0, \\ 0, & \text{if } \Delta_j \leq 0, \end{cases} \quad (23)$$

where  $k_s$  is the segment stiffness,  $c_s$  is the segment damping, and  $[\cdot]^+ = \max(\cdot, 0)$  restricts damping to the stretching phase (preventing energy injection during relaxation). The force on body  $b_{j-1}$  from segment  $j$  is

$$F_j = -T_j \hat{e}_j, \quad (24)$$

with an equal and opposite force  $-F_j$  applied to body  $b_j$ . The net force on each bead is the sum of contributions from its two adjacent segments.

##### 2) Stiffness and Damping Design

The segment stiffness is derived from a maximum-stretch design criterion. Under the nominal static load  $F_{\text{load}} = m_L g / N$  per rope, we require the total rope elongation not to exceed a fraction  $\epsilon_{\text{max}}$  of the rest length:

$$k_{\text{eff}} = \frac{F_{\text{load}}}{L_{\text{rest}} \epsilon_{\text{max}}}, \quad k_s = k_{\text{eff}} \cdot (n_b + 1), \quad (25)$$

where  $k_{\text{eff}}$  is the effective whole-rope stiffness and the factor  $(n_b + 1)$  accounts for the series arrangement of segments. In this work,  $\epsilon_{\text{max}} = 0.15$  (15% maximum stretch). The segment damping is scaled as

$$c_s = c_{\text{ref}} \sqrt{k_s / k_{\text{ref}}}, \quad (26)$$

with reference values  $k_{\text{ref}} = 300 \text{ N/m}$  and  $c_{\text{ref}} = 15 \text{ N}\cdot\text{s/m}$ , ensuring that the damping ratio remains approximately constant across different stiffness levels.

##### 3) Bead Dynamics

Each bead  $b_j$  ( $j = 1, \dots, n_b$ ) has mass  $m_b = m_{\text{rope}}/n_b$ , where  $m_{\text{rope}} = 0.2 \text{ kg}$  is the total rope mass. The beads are modeled as small spheres of radius  $r_b = 0.02 \text{ m}$  for collision purposes. Their dynamics are governed by Newton's second law:

$$m_b \ddot{b}_j = F_j - F_{j+1} - m_b g e_3, \quad (27)$$

where  $F_j$  and  $F_{j+1}$  are the forces from segments  $j$  and  $j+1$ , respectively. The bead-chain naturally captures several physical phenomena absent from rigid-link models: (i) wave propagation along the cable at speed  $\sim \sqrt{k_s L_0 / m_b}$ , (ii) distributed inertia effects with total cable mass  $m_{\text{rope}} = n_b m_b$ ,

and (iii) slack-to-taut transitions when  $\Delta_j$  crosses zero, producing the impulsive loading characteristic of real rope dynamics.

#### 4) Rope Length Uncertainty

To model manufacturing and measurement uncertainty, the rest length of the  $i$ -th rope is sampled from a Gaussian distribution:

$$L_{\text{rest},i} \sim \mathcal{N}(\bar{L}_i, \sigma_{L,i}^2), \quad (28)$$

where the mean lengths  $\bar{L}_i$  and standard deviations  $\sigma_{L,i}$  are specified per quadrotor (e.g.,  $\bar{L} \in \{1.0, 1.1, 0.95\}$  m,  $\sigma_L \in \{0.05, 0.08, 0.06\}$  m). This heterogeneity introduces asymmetric cable forces that the control architecture must accommodate.

#### F. Sensor Models

Each quadrotor carries an onboard sensor suite comprising an IMU, a GPS receiver, and a barometric altimeter. We model each sensor with realistic noise characteristics to evaluate the robustness of the control architecture under practical estimation conditions.

##### 1) Inertial Measurement Unit

The IMU provides 6-DOF measurements at a sample rate of  $f_{\text{IMU}} = 200$  Hz. The accelerometer measures specific force (acceleration minus gravity) in the body frame:

$$\tilde{a}_i = R_i^\top (\ddot{p}_i + g e_3) + b_{a,i} + n_{a,i}, \quad (29)$$

and the gyroscope measures angular velocity in the body frame:

$$\tilde{\omega}_i = \Omega_i + b_{g,i} + n_{g,i}, \quad (30)$$

where  $b_{a,i}, b_{g,i} \in \mathbb{R}^3$  are slowly varying biases and  $n_{a,i}, n_{g,i} \in \mathbb{R}^3$  are zero-mean white Gaussian noise. The noise terms are characterized by their spectral densities:

$$n_{a,i} \sim \mathcal{N}\left(0, \frac{\sigma_a^2}{\Delta t_{\text{IMU}}} I_3\right), \quad n_{g,i} \sim \mathcal{N}\left(0, \frac{\sigma_g^2}{\Delta t_{\text{IMU}}} I_3\right), \quad (31)$$

with accelerometer noise density  $\sigma_a = 0.004 \text{ m/s}^2/\sqrt{\text{Hz}}$  and gyroscope noise density  $\sigma_g = 5 \times 10^{-4} \text{ rad/s}/\sqrt{\text{Hz}}$ .

The biases evolve according to a first-order Gauss–Markov process:

$$\dot{b}_{a,i} = -\frac{1}{\tau_a} b_{a,i} + \eta_{a,i}, \quad \dot{b}_{g,i} = -\frac{1}{\tau_g} b_{g,i} + \eta_{g,i}, \quad (32)$$

where  $\tau_a = \tau_g = 3600$  s are the bias correlation time constants and  $\eta_{a,i}, \eta_{g,i}$  are driving white noise processes with intensities calibrated to the bias instability specifications ( $\sigma_{b,a} = 10^{-3} \text{ m/s}^2$ ,  $\sigma_{b,g} = 10^{-4} \text{ rad/s}$ ). In discrete time, the bias update is

$$b[k+1] = \alpha b[k] + \sqrt{1 - \alpha^2} \sigma_b w[k], \quad \alpha = e^{-\Delta t/\tau}, \quad (33)$$

where  $w[k] \sim \mathcal{N}(0, I_3)$ .

##### 2) GPS Receiver

The GPS receiver provides position measurements at  $f_{\text{GPS}} = 10$  Hz with additive white noise:

$$\tilde{p}_i^{\text{GPS}} = \begin{cases} p_i + n_{p,i}, & \text{with probability } 1 - p_{\text{drop}}, \\ \text{invalid}, & \text{with probability } p_{\text{drop}}, \end{cases} \quad (34)$$

where  $n_{p,i} \sim \mathcal{N}(0, \text{diag}(\sigma_{xy}^2, \sigma_{xy}^2, \sigma_z^2))$  with  $\sigma_{xy} = 0.02$  m and  $\sigma_z = 0.05$  m. The dropout probability  $p_{\text{drop}}$  models intermittent signal loss due to multipath or obstruction.

##### 3) Barometric Altimeter

The barometer provides altitude measurements at  $f_{\text{baro}} = 25$  Hz with a three-component noise model:

$$\tilde{z}_i^{\text{baro}} = z_i + \beta_i + \nu_i + w_{z,i}, \quad (35)$$

where  $\beta_i$  is a slow bias drift,  $\nu_i$  is a correlated noise component, and  $w_{z,i}$  is white measurement noise. The bias drift evolves as a random walk:

$$\dot{\beta}_i = \sigma_\beta \xi_i, \quad \sigma_\beta = 0.002 \text{ m/s}, \quad (36)$$

where  $\xi_i$  is unit white noise. The correlated noise follows a first-order Gauss–Markov process:

$$\dot{\nu}_i = -\frac{1}{\tau_\nu} \nu_i + \eta_{\nu,i}, \quad \tau_\nu = 5.0 \text{ s}, \quad \sigma_\nu = 0.2 \text{ m}, \quad (37)$$

and the white noise has standard deviation  $\sigma_w = 0.3$  m. The measurement is then quantized to a resolution of  $\Delta z = 0.1$  m, consistent with typical MEMS barometers:

$$\tilde{z}_i^{\text{baro}} \leftarrow \Delta z \cdot \text{round}\left(\frac{\tilde{z}_i^{\text{baro}}}{\Delta z}\right). \quad (38)$$

The Drake implementation of these sensor models is described in Section VI-C.

#### G. Cable State Sensing Assumptions

The controller and estimator assume access to two cable-state quantities per drone:

- **Cable tension  $T_i$ :** assumed measured via a uniaxial load cell at the cable attachment point, with additive Gaussian noise  $\sigma_T = 0.5$  N and bias  $\pm 0.1$  N. In simulation,  $T_i$  is computed from the top-segment spring-damper force (23).
- **Cable direction  $q_i \in \mathbb{S}^2$ :** inferred from the attachment-point geometry using the quadrotor's own GPS position and the cable attachment displacement, or measured via a 2-axis encoder at a gimbal mount ( $\sigma_q = 0.02$  rad).

The tension rate  $\dot{T}_i$  is not directly measured; it is estimated via the second-order Butterworth filter (Section V-E) applied to discrete tension samples. These are *assumed* sensing modalities for the controller and estimator design; the simulation uses exact plant-state tension and direction as a proxy for well-calibrated sensors (Section VI-C).

#### H. Error-State Kalman Filter

The heterogeneous sensor measurements are fused via a 15-state Error-State Kalman Filter (ESKF) [11], which propagates at the IMU rate and incorporates GPS and barometer corrections at their respective (lower) rates.

##### 1) State Representation

The nominal state is

$$x = [p^\top, v^\top, \bar{q}^\top, b_a^\top, b_g^\top]^\top \in \mathbb{R}^{16}, \quad (39)$$

where  $p \in \mathbb{R}^3$  is position,  $v \in \mathbb{R}^3$  is velocity,  $\bar{q} \in \mathbb{R}^4$  is the unit quaternion ( $\|\bar{q}\| = 1$ ),  $b_a \in \mathbb{R}^3$  is accelerometer bias, and  $b_g \in \mathbb{R}^3$  is gyroscope bias. The error state, which encodes deviations from the nominal trajectory, is

$$\delta x = [\delta p^\top, \delta v^\top, \delta \theta^\top, \delta b_a^\top, \delta b_g^\top]^\top \in \mathbb{R}^{15}, \quad (40)$$

where  $\delta\theta \in \mathbb{R}^3$  is a minimal (three-parameter) attitude error related to the quaternion error via  $\delta\bar{q} \approx [1, \frac{1}{2}\delta\theta^\top]^\top$ . The use of a 15-dimensional error state avoids the rank deficiency that arises from quaternion normalization constraints.

### 2) Propagation

At each IMU sample, the nominal state is propagated forward using the bias-corrected measurements:

$$p \leftarrow p + v \Delta t + \frac{1}{2} a_W \Delta t^2, \quad (41)$$

$$v \leftarrow v + a_W \Delta t, \quad (42)$$

$$\bar{q} \leftarrow \bar{q} \otimes \delta\bar{q}(\omega_c \Delta t), \quad (43)$$

where  $a_W = R(\bar{q})(\tilde{a} - b_a) - g e_3$  is the world-frame acceleration,  $\omega_c = \tilde{\omega} - b_g$  is the corrected angular velocity,  $\otimes$  denotes quaternion multiplication, and  $\delta\bar{q}(\phi)$  is the quaternion corresponding to the rotation vector  $\phi$ .

The error-state covariance  $P \in \mathbb{R}^{15 \times 15}$  is propagated via

$$P \leftarrow \Phi P \Phi^\top + Q_d, \quad (44)$$

where  $\Phi \approx I_{15} + F \Delta t$  is the first-order discrete state transition matrix and  $Q_d = G Q_c G^\top \Delta t$  is the discrete process noise. The continuous-time error-state Jacobian  $F \in \mathbb{R}^{15 \times 15}$  has the structure

$$F = \begin{bmatrix} 0_3 & I_3 & 0_3 & 0_3 & 0_3 \\ 0_3 & 0_3 & -R[\tilde{a} - b_a] & -R & 0_3 \\ 0_3 & 0_3 & -[\tilde{\omega} - b_g] & 0_3 & -I_3 \\ 0_3 & 0_3 & 0_3 & 0_3 & 0_3 \\ 0_3 & 0_3 & 0_3 & 0_3 & 0_3 \end{bmatrix}, \quad (45)$$

and the noise input matrix  $G \in \mathbb{R}^{15 \times 12}$  maps the four noise sources (accelerometer, gyroscope, accelerometer bias random walk, gyroscope bias random walk) to the error state:

$$G = \begin{bmatrix} 0_3 & 0_3 & 0_3 & 0_3 \\ -R & 0_3 & 0_3 & 0_3 \\ 0_3 & -I_3 & 0_3 & 0_3 \\ 0_3 & 0_3 & I_3 & 0_3 \\ 0_3 & 0_3 & 0_3 & I_3 \end{bmatrix}. \quad (46)$$

The continuous-time process noise spectral density is  $Q_c = \text{diag}(\sigma_a^2 I_3, \sigma_g^2 I_3, \sigma_{b_a}^2 I_3, \sigma_{b_g}^2 I_3) \in \mathbb{R}^{12 \times 12}$ .

### 3) Measurement Updates

#### a) GPS Position Update

When a valid GPS measurement  $\tilde{p}^{\text{GPS}}$  is available, the measurement model is  $h_{\text{GPS}}(x) = p$ , giving the observation Jacobian  $H_{\text{GPS}} = [I_3, 0_{3 \times 12}] \in \mathbb{R}^{3 \times 15}$ . The Kalman gain, innovation, and Joseph-form covariance update are

$$K = P H_{\text{GPS}}^\top (H_{\text{GPS}} P H_{\text{GPS}}^\top + R_{\text{GPS}})^{-1}, \quad (47)$$

$$\delta x = K(\tilde{p}^{\text{GPS}} - p), \quad (48)$$

$$P \leftarrow (I - K H_{\text{GPS}}) P (I - K H_{\text{GPS}})^\top + K R_{\text{GPS}} K^\top, \quad (49)$$

where  $R_{\text{GPS}} = \text{diag}(\sigma_{xy}^2, \sigma_{xz}^2, \sigma_z^2)$ .

#### b) Barometer Altitude Update

The barometer measurement model is  $h_{\text{baro}}(x) = e_3^\top p$ , yielding  $H_{\text{baro}} = [0, 0, 1, 0, \dots, 0] \in \mathbb{R}^{1 \times 15}$  and scalar innovation covariance  $S = H_{\text{baro}} P H_{\text{baro}}^\top + \sigma_{\text{baro}}^2$  with  $\sigma_{\text{baro}} = 0.3 \text{ m}$ .

### c) Error Injection and Reset

After each update, the error state  $\delta x$  is injected into the nominal state:

$$p \leftarrow p + \delta p, \quad v \leftarrow v + \delta v, \quad (50)$$

$$\bar{q} \leftarrow \bar{q} \otimes \delta\bar{q}(\delta\theta), \quad \bar{q} \leftarrow \bar{q} / \|\bar{q}\|, \quad (51)$$

$$b_a \leftarrow b_a + \delta b_a, \quad b_g \leftarrow b_g + \delta b_g, \quad (52)$$

and the error state is conceptually reset to zero.

#### I. Wind Disturbance Model

Wind disturbances are generated by a Dryden turbulence model conforming to MIL-F-8785C [12]. The wind velocity at each quadrotor is decomposed as

$$w_i(t) = \bar{w} + w_i^{\text{turb}}(t) + w^{\text{gust}}(t), \quad (53)$$

where  $\bar{w} \in \mathbb{R}^3$  is the mean wind vector,  $w_i^{\text{turb}}$  is the stochastic turbulence component, and  $w^{\text{gust}}$  represents discrete gust events.

##### 1) Dryden Turbulence

The turbulence component along each axis ( $u$ : longitudinal,  $v$ : lateral,  $w$ : vertical) is generated by passing white noise through a first-order forming filter with transfer function

$$H_\alpha(s) = \sigma_\alpha \sqrt{\frac{2V}{L_\alpha}} \cdot \frac{1}{s + V/L_\alpha}, \quad \alpha \in \{u, v, w\}, \quad (54)$$

where  $\sigma_\alpha$  is the turbulence intensity,  $L_\alpha$  is the turbulence length scale, and  $V$  is a reference airspeed. The discrete-time approximation is

$$x_\alpha[k+1] = e^{-\Delta t/\tau_\alpha} x_\alpha[k] + \sigma_\alpha \sqrt{1 - e^{-2\Delta t/\tau_\alpha}} w[k], \quad (55)$$

with time constant  $\tau_\alpha = L_\alpha/V$ , yielding colored noise with the correct power spectral density. The default parameters are  $\sigma_u = \sigma_v = 0.5 \text{ m/s}$ ,  $\sigma_w = 0.25 \text{ m/s}$ ,  $L_u = L_v = 200 \text{ m}$ ,  $L_w = 50 \text{ m}$ , and  $V = 5 \text{ m/s}$ .

##### 2) Altitude Dependence

At low altitudes, turbulence intensity is scaled according to

$$\sigma_\alpha(h) = \sigma_\alpha^{\text{ref}} \cdot \left( \frac{h}{h_{\text{ref}}} \right)^{1/6}, \quad (56)$$

where  $h_{\text{ref}} = 20 \text{ m}$  is the reference altitude. This produces reduced turbulence near the ground surface and full intensity at or above  $h_{\text{ref}}$ , consistent with the low-altitude turbulence model of MIL-F-8785C [12].

##### 3) Spatial Correlation

Drones in close proximity experience correlated wind. The spatial correlation between the turbulence components at positions  $p_i$  and  $p_j$  decays exponentially:

$$\rho(p_i, p_j) = \exp\left(-\frac{\|p_i - p_j\|}{\ell_c}\right), \quad (57)$$

where  $\ell_c = 10 \text{ m}$  is the correlation length scale. The correlated noise for drone  $i$  is computed as a weighted average of independent noise samples:

$$\tilde{w}_i = \frac{w_i + \sum_{j \neq i} \rho_{ij} w_j}{1 + \sum_{j \neq i} \rho_{ij}}, \quad (58)$$

where  $w_j$  are independent standard normal samples and  $\rho_{ij} = \rho(p_i, p_j)$ .

TABLE II: Simulation and Physical Parameters

Parameter	Symbol	Value
<i>Quadrrotor</i>		
Mass	$m_Q$	1.5 kg
Dimensions	$N$	$0.30 \times 0.30 \times 0.10$ m
Number of agents	$r_f$	3
Formation radius		0.6 m
<i>Payload</i>		
Mass	$m_L$	3.0 kg
Radius	$r_L$	0.15 m
Ground friction ( $\mu_s / \mu_k$ )		0.5 / 0.3
<i>Cable (per rope)</i>		
Number of beads	$n_b$	8
Total rope mass	$m_{\text{rope}}$	0.2 kg
Maximum stretch	$\epsilon_{\max}$	15%
Stiffness ref. / damping ref.	$k_{\text{ref}} / c_{\text{ref}}$	300 / 15
<i>IMU (200 Hz)</i>		
Accel. noise density	$\sigma_a$	$0.004 \text{ m/s}^2 / \sqrt{\text{Hz}}$
Gyro noise density	$\sigma_g$	$5 \times 10^{-4} \text{ rad/s} / \sqrt{\text{Hz}}$
Bias time constant	$\tau_b$	3600 s
<i>GPS (10 Hz)</i>		
Horizontal noise	$\sigma_{xy}$	0.02 m
Vertical noise	$\sigma_z$	0.05 m
<i>Barometer (25 Hz)</i>		
White noise	$\sigma_w$	0.3 m
Correlated noise	$\sigma_v$	0.2 m
Drift rate	$\sigma_\beta$	0.002 m/s
Quantization	$\Delta z$	0.1 m
<i>Wind (Dryden)</i>		
Longitudinal / lateral	$\sigma_u, \sigma_v$	0.5 m/s
Vertical	$\sigma_w$	0.25 m/s
Length scales	$L_u, L_v / L_w$	200 / 50 m
<i>Simulation</i>		
Time step	$\Delta t_{\text{sim}}$	$2 \times 10^{-4}$ s
Duration	—	50 s

#### 4) Gust Model

Discrete gust events are optionally superimposed with a trapezoidal temporal profile:

$$w^{\text{gust}}(t) = A_g \hat{d}_g \cdot \begin{cases} (t - t_0)/t_r, & t_0 \leq t < t_0 + t_r \\ 1, & t_0 + t_r \leq t < t_0 + t_r + t_h \\ 1 - (t - t_0 - t_r - t_h)/t_f, & t_0 + t_r + t_h \leq t < t_0 + t_r + t_h + t_f \\ 0, & \text{otherwise,} \end{cases} \quad (59)$$

where  $A_g$  is the gust magnitude (up to 5 m/s),  $\hat{d}_g \in \mathbb{S}^2$  is the gust direction (predominantly horizontal), and  $t_r = 1.0$  s,  $t_h = 2.0$  s,  $t_f = 1.5$  s are the rise, hold, and fall times, respectively. Gusts are triggered stochastically with a mean inter-arrival time of 30 s. Implementation details of the wind disturbance system are given in Section VI-D.

#### J. Simulation Parameters

Table II collects all physical and sensor parameters used throughout the paper. The Drake-based simulation environment, multi-body construction pipeline, timing architecture, and system interconnection are described in Section VI.

### III. GPAC CONTROL ARCHITECTURE

This section presents the *Geometric Position and Attitude Control* (GPAC) framework, a four-layer hierarchical controller for cooperative cable-suspended transport. The architecture exploits the geometric structure of the configuration manifold (15) by assigning each physical degree of freedom to the appropriate control layer, operating at progressively higher bandwidths from position tracking through disturbance rejection. Fig. 1 illustrates the information flow.

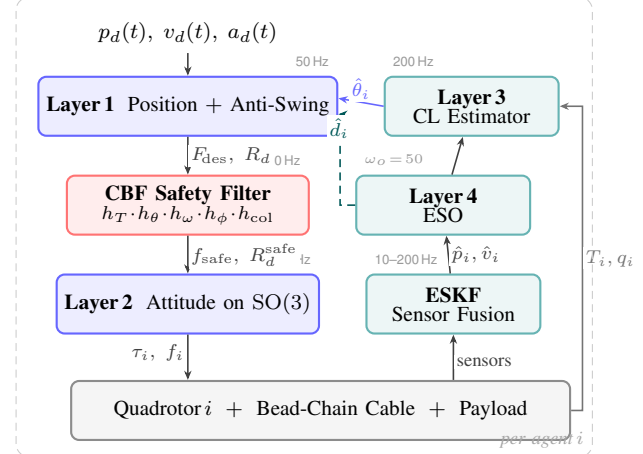


Fig. 1: GPAC hierarchical architecture for a single agent. **Left column** (blue): control cascade—Layer 1 computes the desired force  $F_{\text{des}}$  and extracts  $R_d$ ; the CBF safety filter (red) enforces tautness, angle, tilt, and collision constraints; Layer 2 tracks the safe attitude on  $\text{SO}(3)$ . **Right column** (teal): estimation cascade—the ESKF fuses IMU/GPS/barometer; Layer 4 (ESO, continuous-time,  $\omega_o = 50$  rad/s) estimates lumped disturbances  $\hat{d}_i$ ; Layer 3 (concurrent learning, 50 Hz) estimates the payload mass share  $\hat{\theta}_i \rightarrow m_L/N$ . Dashed arrows denote feedforward paths. Each agent executes this pipeline independently.

#### a) Information pattern

Each agent  $i$  receives at runtime: (i) a shared reference trajectory  $p_d(t)$  (broadcast once before flight or via a low-bandwidth downlink); (ii) its own IMU, GPS, and barometer measurements; (iii) local cable tension  $T_i$  and direction  $\dot{q}_i$  from attachment-point sensors (Section II-G). For the collision avoidance barrier  $h_{\text{col},ij}$ , neighbor positions  $p_j$  are obtained via GPS broadcast (each drone transmits its own position at the GPS rate of 10 Hz). No payload state, no other agent's cable state, and no centralized coordinator are required.

#### A. Layer 1: Position Tracking and Anti-Swing Control

The outermost layer computes a desired total thrust vector  $F_{\text{des},i} \in \mathbb{R}^3$  for each quadrotor by combining trajectory tracking, cable tension compensation, anti-swing regulation on  $\mathbb{S}^2$ , and disturbance feedforward. This layer operates at the effective position-control bandwidth of approximately 50 Hz.

##### 1) Trajectory Tracking

Let  $p_{d,i}(t)$ ,  $v_{d,i}(t)$ , and  $a_{d,i}(t)$  denote the desired position, velocity, and acceleration for quadrotor  $i$ , generated from a shared waypoint trajectory with individual formation offsets (Section II-J). Define the tracking errors  $e_{p_i} = p_i - p_{d,i}$  and  $e_{v_i} = v_i - v_{d,i}$ , and the integral error  $e_{I_i} = \int_0^t e_{p_i}(\tau) d\tau$  with per-axis anti-windup clamping  $|e_{I_i,k}| \leq \bar{e}_I = 2.0$ . The PID feedback force is

$$F_{\text{fb},i} = -K_p e_{p_i} - K_d e_{v_i} - K_i e_{I_i}, \quad (60)$$

where  $K_p = \text{diag}(6, 6, 8)$ ,  $K_d = \text{diag}(8, 8, 10)$ , and  $K_i = \text{diag}(0.1, 0.1, 0.2)$  are diagonal gain matrices. The feedforward force compensates gravity and the nominal trajectory

acceleration:

$$F_{\text{ff},i} = m_Q (a_{d_i} + g e_3). \quad (61)$$

### 2) Cable Tension Compensation

During cooperative transport, the cable exerts a downward force on each quadrotor. To prevent the position controller from treating this force as a disturbance, we add a tension feedforward term:

$$F_{\text{cable},i} = \kappa_T T_i q_i, \quad (62)$$

where  $T_i$  is the measured top-segment cable tension,  $q_i \in \mathbb{S}^2$  is the measured cable direction (pointing from the payload toward the quadrotor), and  $\kappa_T = 1.0$  is the compensation gain. During the pickup phase, a ramped tension target prevents impulsive loading: the target tension increases linearly from 0 to  $T_{\text{target}} = m_L g / N$  over a duration  $t_{\text{ramp}} = 2.0$  s after the cable first becomes taut (detected when  $T_i \geq T_{\text{detect}} = 1.0$  N). A proportional feedback term  $K_{T_p}(T_{\text{target}} - T_i)$  with  $K_{T_p} = 0.5$  and an altitude adjustment  $\Delta z_i = K_z(T_{\text{target}} - T_i)$  with  $K_z = 0.003$  m/N (clamped to  $\pm 0.5$  m) smooth the transition.

### 3) Anti-Swing Control on $\mathbb{S}^2$

Pendular oscillations of the cable-suspended payload degrade tracking performance and can excite resonances in the bead-chain model. We suppress these oscillations using a control law defined intrinsically on  $\mathbb{S}^2$  [3]. Let  $q_{d,i} \in \mathbb{S}^2$  be the desired cable direction (typically  $-e_3$ , i.e., hanging vertically downward). The cable direction error  $e_{q_i}$  (20) lies in the tangent space at  $q_i$  and vanishes if and only if  $q_i = q_{d,i}$ . Let  $\omega_{q_i}$  denote the cable angular velocity projected onto  $T_{q_i}\mathbb{S}^2$  via  $\omega_{q_i} \leftarrow P(q_i)\omega_{q_i}$ . The anti-swing control force is

$$F_{\text{swing},i} = k_q e_{q_i} - k_\omega \omega_{q_i}, \quad (63)$$

with  $k_q = 4.0$  and  $k_\omega = 2.0$ . The proportional term steers  $q_i$  toward  $q_{d,i}$  along the geodesic on  $\mathbb{S}^2$ , and the derivative term damps the cable swing rate. Together, these terms reduce the configuration error  $\Psi_{q_i} = 1 - q_{d,i}^\top q_i$  monotonically when no external perturbation is present.

### 4) Disturbance Feedforward

The Extended State Observer (Layer 4, Section III-D) provides an estimate  $\hat{d}_i \in \mathbb{R}^3$  of the lumped disturbance acceleration acting on quadrotor  $i$ . This estimate is fed forward as

$$F_{\text{eso},i} = m_Q \hat{d}_i. \quad (64)$$

### 5) Total Thrust Vector and Desired Rotation

The total desired thrust vector is the sum of all contributions:

$$F_{\text{des},i} = F_{\text{ff},i} + F_{\text{fb},i} + F_{\text{cable},i} + F_{\text{swing},i} + F_{\text{eso},i}, \quad (65)$$

subject to saturation  $\|F_{\text{des},i}\| \in [f_{\min}, f_{\max}]$  with  $f_{\min} = 0$  and  $f_{\max} = 150$  N. The scalar thrust magnitude is  $f_i = \|F_{\text{des},i}\|$ .

The desired rotation matrix  $R_{d,i} \in \text{SO}(3)$  is constructed from  $F_{\text{des},i}$  and a desired yaw angle  $\psi_{d,i}$  following [1]:

$$b_{3,c} = \frac{F_{\text{des},i}}{\|F_{\text{des},i}\|}, \quad b_{1,d} = \begin{bmatrix} \cos \psi_{d,i} \\ \sin \psi_{d,i} \\ 0 \end{bmatrix}, \quad (66)$$

$$b_{2,c} = \frac{b_{3,c} \times b_{1,d}}{\|b_{3,c} \times b_{1,d}\|}, \quad b_{1,c} = b_{2,c} \times b_{3,c}, \quad (67)$$

$$R_{d,i} = [b_{1,c} \ b_{2,c} \ b_{3,c}]. \quad (68)$$

This construction ensures that the body  $z$ -axis aligns with the desired thrust direction and the heading aligns with  $\psi_{d,i}$  as closely as possible, producing a rotation matrix that is always well-defined except when  $b_{3,c}$  is parallel to  $b_{1,d}$  (handled by a fallback in the implementation).

### B. Layer 2: Geometric Attitude Control on $\text{SO}(3)$

Given the desired rotation  $R_{d,i}$  from Layer 1, the inner attitude loop computes body-frame control torques using the geometric tracking controller of Lee et al. [1]. This layer operates at 200 Hz and provides almost-global exponential stability on  $\text{SO}(3)$  without the kinematic singularities inherent in Euler-angle representations.

#### 1) Error Functions on $\text{SO}(3)$

The attitude error vector  $e_{R,i}$  (18) and the angular velocity error

$$e_{\Omega,i} = \Omega_i - R_i^\top R_{d,i} \Omega_{d,i}, \quad (69)$$

where  $\Omega_{d,i} \in \mathbb{R}^3$  is the desired angular velocity in the body frame (set to zero in the current implementation, as no angular velocity feedforward is computed), are the primary error quantities. The attitude error  $e_{R,i}$  is related to the configuration error function  $\Psi_{R,i} = \frac{1}{2} \text{tr}(I - R_i^\top R_i)$  via

$$e_{R,i} = -\nabla_{R,i} \Psi_{R,i}, \quad (70)$$

which provides a natural gradient descent direction on  $\text{SO}(3)$  [1].

#### 2) Geometric Torque Law

The full geometric control torque on  $\text{SO}(3)$  is

$$\tau_i = -k_R e_{R,i} - k_\Omega e_{\Omega,i} + \Omega_i \times J \Omega_i - J (\widehat{\Omega_i} R_i^\top R_{d,i} \Omega_{d,i} - R_i^\top R_{d,i} \dot{\Omega}_{d,i}), \quad (71)$$

where the first two terms are the proportional-derivative control, the third is the gyroscopic compensation, and the last term is the feedforward. Under the simplification  $\Omega_{d,i} \approx 0$  (valid when the desired thrust direction changes slowly relative to the attitude bandwidth), the control law reduces to

$$\tau_i = -k_R e_{R,i} - k_\Omega e_{\Omega,i}, \quad (72)$$

with  $k_R = 8.0$  and  $k_\Omega = 1.5$ . Each component is saturated to  $|\tau_{i,k}| \leq \bar{\tau} = 10.0$  N·m. This saturation limit is conservative for the simulated platform; the observed peak torque of 1.74 N·m (Section VII-G) remains well within this bound. For specific hardware,  $\bar{\tau}$  should be set to the platform's actuator limit.

#### 3) Stability Properties

Define the Lyapunov function candidate [1]

$$V_R = \frac{1}{2} k_R \Psi_{R,i} + \frac{1}{2} e_{\Omega,i}^\top J e_{\Omega,i} + c e_{R,i}^\top J e_{\Omega,i}, \quad (73)$$

for a sufficiently small cross-term coefficient  $c > 0$ . Under the simplified control law (72), the time derivative satisfies

$$\dot{V}_R \leq -\lambda_{\min}(W) (\|e_{R,i}\|^2 + \|e_{\Omega,i}\|^2) \quad (74)$$

for an appropriate positive-definite matrix  $W = W(k_R, k_\Omega, J)$ , provided the initial attitude error satisfies

$\Psi_{R_i}(0) < 2$  (i.e., the initial rotation is less than  $180^\circ$  from the desired). This gives *almost-global exponential stability* of  $(R_i, \Omega_i) = (R_{d_i}, \Omega_{d_i})$  on the dense open set  $\{\Psi_{R_i} < 2\} \subset \text{SO}(3)$  [1].

#### 4) Cascaded Stability

The two-layer cascade (position→attitude) inherits stability from the timescale separation: the attitude loop converges an order of magnitude faster than the position loop ( $K_p/m_Q \approx 5 \text{ Hz}$  effective bandwidth). Standard singular perturbation arguments [14] guarantee that the composite system is locally exponentially stable when the bandwidth ratio exceeds a computable threshold, and the anti-swing control on  $\mathbb{S}^2$  provides additional damping of the slow cable modes.

#### C. Layer 3: Concurrent Learning Estimator

The payload mass  $m_L$  is unknown and must be estimated online. Each quadrotor independently estimates its share  $\hat{\theta}_i \approx m_L/N$  using only local measurements—cable tension, cable direction, and the estimated load acceleration. A concurrent learning adaptive law [6], [7] augments the standard gradient-descent update with stored historical data, guaranteeing parameter convergence *without* the persistent excitation condition required by classical adaptive control [15]. This is critical because cooperative hover provides insufficient excitation for classical adaptive laws.

The estimated parameter feeds into the position controller (Layer 1) as the gravity compensation term  $\hat{\theta}_i(g e_3 + \ddot{p}_d^L)$ . The full derivation of the regressor model, adaptation law, history buffer management, parameter projection, and convergence analysis is presented in Section IV-D.

#### D. Layer 4: Extended State Observer

The innermost estimation layer is a continuous-time third-order Extended State Observer (ESO) with bandwidth  $\omega_o = 50 \text{ rad/s}$ , based on the active disturbance rejection control (ADRC) framework of Han and Guo [16], [17]. The ESO estimates position, velocity, and the total *lumped disturbance* (including modeling errors, unmodeled dynamics, and external forces) from position measurements alone, without requiring a detailed plant model.

##### 1) Observer Structure

For each spatial axis  $k \in \{x, y, z\}$ , the ESO models the translational dynamics as a double integrator with an unknown disturbance:

$$\ddot{p}_k = b_0 u_k + d_k(t), \quad (75)$$

where  $u_k$  is the control force component (N) along axis  $k$ ,  $b_0 = 1/m_Q = 0.667 \text{ kg}^{-1}$  is the nominal input gain mapping force to acceleration, and  $d_k(t)$  is the lumped disturbance. The ESO is a third-order observer:

$$\dot{\hat{z}}_{1k} = \hat{z}_{2k} + \ell_1 (p_k - \hat{z}_{1k}), \quad (76)$$

$$\dot{\hat{z}}_{2k} = \hat{z}_{3k} + \ell_2 (p_k - \hat{z}_{1k}) + b_0 u_k, \quad (77)$$

$$\dot{\hat{z}}_{3k} = \ell_3 (p_k - \hat{z}_{1k}), \quad (78)$$

where  $\hat{z}_{1k}$ ,  $\hat{z}_{2k}$ , and  $\hat{z}_{3k}$  estimate position, velocity, and disturbance, respectively, and  $\ell_1, \ell_2, \ell_3$  are the observer gains.

##### 2) Gain Design: Bandwidth Parameterization

The gains are chosen to place all three observer poles at  $-\omega_o$ , yielding

$$\ell_1 = 3\omega_o, \quad \ell_2 = 3\omega_o^2, \quad \ell_3 = \omega_o^3, \quad (79)$$

where  $\omega_o = 50 \text{ rad/s}$  is the observer bandwidth. This *bandwidth parameterization* [17] reduces the tuning to a single scalar: increasing  $\omega_o$  improves disturbance tracking but amplifies measurement noise, while decreasing  $\omega_o$  provides better noise rejection at the cost of slower disturbance estimation. The characteristic polynomial of the observer error dynamics is  $(\lambda + \omega_o)^3 = 0$ , giving a uniform settling time of  $t_s \approx 5/\omega_o = 0.1 \text{ s}$ .

##### 3) Disturbance Estimate

The disturbance estimate  $\hat{d}_i = [\hat{z}_{3x}, \hat{z}_{3y}, \hat{z}_{3z}]^\top$  is saturated component-wise to  $|\hat{d}_{i,k}| \leq \bar{d} = 20 \text{ m/s}^2$  to prevent unbounded estimates during transients. This estimate is fed forward via (64), providing feedforward disturbance compensation with estimation lag bounded by  $5/\omega_o = 0.1 \text{ s}$ .

##### 4) Convergence Properties

Under the assumption that  $d_k(t)$  is differentiable with bounded derivative, the estimation errors  $\tilde{z}_{jk} = z_{jk} - \hat{z}_{jk}$  satisfy [17]

$$|\tilde{z}_{jk}(t)| \leq c_j \omega_o^{j-4} \sup_{\tau \leq t} |\dot{d}_k(\tau)| + \mathcal{O}(e^{-\omega_o t}), \quad j = 1, 2, 3, \quad (80)$$

for constants  $c_j > 0$ . In particular, the disturbance estimation error scales as  $\mathcal{O}(\sup |\dot{d}| / \omega_o)$ , showing that faster observer bandwidth yields tighter estimation.

#### E. CBF Safety Filter

A Control Barrier Function (CBF) safety filter [8], [9] is applied as a minimally invasive post-processing step to enforce operational constraints while staying as close to the nominal GPAC control signal as possible.

##### 1) Barrier Function Design

We define five barrier functions encoding the physical safety constraints. For each constraint  $h : \mathbb{R}^n \rightarrow \mathbb{R}$ , the safe set is  $\mathcal{C} = \{x \mid h(x) \geq 0\}$ :

###### a) Cable Tautness

The most critical constraint ensures that cable tension remains within bounds:

$$h_T^{\text{low}} = T_i - T_{\min}, \quad h_T^{\text{up}} = T_{\max} - T_i, \quad (81)$$

with  $T_{\min} = 2.0 \text{ N}$  and  $T_{\max} = 60.0 \text{ N}$ .

###### b) Cable Angle

The cable deviation from vertical is bounded:

$$h_\theta = \cos \theta_{\max} - \cos \theta_i, \quad \theta_i = \arccos(q_i^\top (-e_3)), \quad (82)$$

with  $\theta_{\max} = 0.6 \text{ rad} (\approx 34^\circ)$ .

###### c) Swing Rate

The cable angular velocity is bounded:

$$h_\omega = \omega_{\max}^2 - \|\omega_{q_i}\|^2, \quad (83)$$

with  $\omega_{\max} = 1.5 \text{ rad/s}$ .

###### d) Quadrotor Tilt

The tilt angle is constrained:

$$h_{\text{tilt}} = \cos \phi_{\max} - \cos \phi_i, \quad \phi_i = \arccos(e_3^\top R_i e_3), \quad (84)$$

TABLE III: CBF Safety Filter Parameters

Constraint	$\alpha_j$	Threshold
Cable tautness (lower)	3.0	$T_{\min} = 2.0 \text{ N}$
Cable tautness (upper)	3.0	$T_{\max} = 60.0 \text{ N}$
Cable angle	2.0	$\theta_{\max} = 0.6 \text{ rad}$
Swing rate	1.5	$\omega_{\max} = 1.5 \text{ rad/s}$
Quadrotor tilt	4.0	$\phi_{\max} = 0.5 \text{ rad}$
Collision avoidance	3.0	$d_{\min} = 0.8 \text{ m}$

with  $\phi_{\max} = 0.5 \text{ rad} (\approx 29^\circ)$ .

#### e) Inter-Agent Separation

Collision avoidance between quadrotors:

$$h_{\text{col},ij} = \|p_i - p_j\|^2 - d_{\min}^2, \quad (85)$$

with  $d_{\min} = 0.8 \text{ m}$ .

*Remark 3.1 (Physical rationale for safety constraints):*

Each barrier function corresponds to a specific operational hazard: cable tautness prevents uncontrolled payload swing upon re-engagement after slack; cable angle limits prevent entanglement and maintain a controllable suspension geometry; swing rate bounds prevent resonant excitation of the bead-chain cable modes; tilt limits ensure sufficient vertical thrust margin for altitude maintenance; and collision avoidance prevents catastrophic inter-agent contact.

#### 2) Safety QP and Formal Analysis

The safety filter solves a quadratic program at each control cycle that minimally modifies the nominal thrust to maintain all barrier constraints. The full QP formulation, Lie derivative derivations for each transport-specific constraint, Higher-Order CBF treatment of relative-degree-two constraints (cable angle, tilt, collision avoidance), the Butterworth-filtered tension rate estimation, the input-to-state safety guarantee incorporating the ESO disturbance estimate, and the compatibility proof with the geometric attitude controller are presented in Section V.

### IV. DECENTRALIZED ADAPTIVE ESTIMATION

A defining feature of the proposed architecture is that each quadrotor estimates the system state using only locally available information—its own sensors and the cable connecting it to the payload—without explicit inter-agent communication. Intuitively, each drone asks a single question: “how heavy is my share of the payload?” It answers by observing its cable tension and angle—when the cable is taut, the vertical component of the tension divided by the sensed acceleration magnitude directly reveals the per-drone mass share  $\theta_i = m_L/N$ . Past observations are stored and replayed so that even during hover, when excitation is minimal, the answer keeps improving.

This section presents three estimation subsystems: (i) an Error-State Kalman Filter (ESKF) for onboard navigation, (ii) a geometric load-state estimator derived from cable kinematics, and (iii) an adaptive payload-mass estimator based on concurrent learning.

#### A. Per-Drone Navigation: Error-State Kalman Filter

The ESKF introduced in Section II-H provides each quadrotor  $i$  with a fused estimate of its own position  $\hat{p}_i$ , velocity  $\hat{v}_i$ , attitude  $\hat{R}_i$ , and sensor biases  $\hat{b}_{a,i}$ ,  $\hat{b}_{g,i}$  from the onboard IMU (200 Hz), GPS (10 Hz), and barometer (25 Hz). Since the ESKF formulation was detailed in Section II-H,

we focus here on two aspects relevant to the decentralized estimation pipeline.

#### 1) Interface with Control and Estimation Layers

The ESKF provides the following quantities to downstream modules:

- *Position and velocity estimates* ( $\hat{p}_i, \hat{v}_i$ ): used by the GPAC position controller (Layer 1, Section III-A), the ESO (Layer 4, Section III-D), and the decentralized load estimator (Section IV-B).
- *Attitude estimate*  $\hat{R}_i$ : used by the geometric attitude controller (Layer 2, Section III-B).
- *Covariance diagonal*  $\text{diag}(P_i)$ : used by the load estimator to weight the cable-based measurement update.

When the estimated state port is connected to the GPAC controller, the controller uses  $(\hat{p}_i, \hat{v}_i)$  in place of the plant-state position and velocity, closing the loop through the estimator rather than through ground truth. This architecture ensures that all control and estimation decisions are based solely on sensor-derived information.

#### 2) GPS Dropout Resilience

The GPS sensor model (Section II-F) includes a configurable dropout probability  $p_{\text{drop}}$ . During GPS outages, the ESKF prediction step (41)–(43) continues to propagate the state using IMU data, and the covariance grows according to (44). The barometer update provides altitude observability at 25 Hz even when GPS is unavailable, preventing unbounded vertical drift. Horizontal drift during outages is bounded by the accelerometer bias stability ( $\sigma_{b_a} = 10^{-3} \text{ m/s}^2$ , time constant  $\tau_a = 3600 \text{ s}$ ), yielding worst-case position error growth of approximately  $\sigma_{b_a} t^2/2$ .

#### B. Decentralized Load-State Estimation

Each quadrotor estimates the payload position  $\hat{p}_{L,i}$  and velocity  $\hat{v}_{L,i}$  from its own position estimate and the cable geometric relationship, without communicating with the other agents. This provides the reference signal for the trajectory tracking and the regressor for the adaptive mass estimator.

#### 1) Geometric Measurement Model

When the cable connecting quadrotor  $i$  to the payload is taut, the payload position can be computed geometrically. Let  $n_i \in \mathbb{S}^2$  denote the unit vector pointing from the quadrotor toward the load attachment point, and let  $L_i$  denote the cable rest length. The geometric measurement is

$$z_{p_i} = \hat{p}_i - L_i n_i, \quad (86)$$

which estimates  $p_L + R_L \rho_i^L$  (the world-frame attachment point on the payload). For the current system with attachment points near the payload center of mass,  $R_L \rho_i^L \approx p_L$ , and (86) directly estimates the load position.

The quality of this geometric estimate depends on (i) the accuracy of  $\hat{p}_i$  from the ESKF, (ii) the cable direction measurement noise, and (iii) the cable sag, which introduces a systematic bias proportional to the catenary departure from a straight line. Under tension  $T_i$ , the sag is  $\delta_{\text{sag}} \approx m_{\text{rope}} g L_i / (8T_i)$ , which is small when the cable is taut.

#### 2) Kalman Filter Formulation

Each drone maintains a discrete-time Kalman filter with state  $\hat{x}_{L,i} = [\hat{p}_{L,i}^\top, \hat{v}_{L,i}^\top]^\top \in \mathbb{R}^6$  and diagonal covariance

$P_i \in \mathbb{R}^{6 \times 6}$  (stored as a 6-vector for efficiency).

#### a) Prediction Step

The load dynamics are modeled as a constant-velocity process:

$$\hat{p}_{L,i}^- = \hat{p}_{L,i} + \hat{v}_{L,i} \Delta t, \quad (87)$$

$$\hat{v}_{L,i}^- = (1 - \beta_v) \hat{v}_{L,i} + \beta_v \hat{v}_i, \quad (88)$$

where  $\beta_v = 0.05$  is a velocity damping factor that gently biases the load velocity estimate toward the quadrotor velocity (a quasi-static assumption valid during slow transport). The predicted covariance grows as

$$P_i^- = P_i + \text{diag}(\sigma_{Q_p}^2 \Delta t, \sigma_{Q_v}^2 \Delta t), \quad (89)$$

with position process noise  $\sigma_{Q_p} = 0.05 \text{ m}$  and velocity process noise  $\sigma_{Q_v} = 0.2 \text{ m/s}$ .

#### b) Measurement Update

The geometric measurement (86) is fused via a scalar Kalman gain per axis:

$$K_{i,k} = \frac{\kappa_c P_{i,k}^-}{P_{i,k}^- + R_k}, \quad k \in \{x, y, z\}, \quad (90)$$

where  $\kappa_c = 0.9$  is the cable trust factor and the measurement variance is

$$R_k = \sigma_{\text{cat}}^2 + \sigma_n^2 L_i^2 + \sigma_L^2, \quad (91)$$

composed of catenary model uncertainty ( $\sigma_{\text{cat}} = 0.15 \text{ m}$ ), cable direction noise ( $\sigma_n = 0.02 \text{ rad}$ , scaled by cable length), and length uncertainty ( $\sigma_L = 0.01 \text{ m}$ ). The measurement noise is modulated by the cable tension via a confidence factor:

$$\xi_T = \min\left(1, \frac{T_i}{T_{\text{conf}}}\right), \quad R_k \leftarrow \frac{R_k}{0.1 + 0.9 \xi_T}, \quad (92)$$

with  $T_{\text{conf}} = 20 \text{ N}$ . When the cable is slack ( $T_i \approx 0$ ), the measurement variance increases dramatically and the filter relies primarily on the prediction.

#### c) Outlier Rejection

The innovation  $\nu_i = z_{p_i} - \hat{p}_{L,i}^-$  is validated against the expected standard deviation:

$$\|\nu_i\| < \kappa_\nu \sqrt{\frac{1}{3} \mathbf{1}^\top P_i^- + R_k}, \quad \kappa_\nu = 3.0. \quad (93)$$

Measurements exceeding this gate are rejected, preventing cable whip or GPS outliers from corrupting the load estimate.

#### d) State and Covariance Update

If the measurement passes validation:

$$\hat{p}_{L,i,k} \leftarrow \hat{p}_{L,i,k}^- + K_{i,k} \nu_{i,k}, \quad (94)$$

$$P_{i,k} \leftarrow (1 - K_{i,k}) P_{i,k}^-, \quad (95)$$

for each axis  $k$ . The velocity estimate is additionally blended with the innovation-implied velocity:

$$\hat{v}_{L,i} \leftarrow (1 - \alpha_v) \hat{v}_{L,i}^- + \alpha_v \frac{\nu_i}{\Delta t}, \quad (96)$$

with blending factor  $\alpha_v = 0.3$ . The covariance is bounded element-wise to  $[10^{-6}, 100]$  to prevent numerical issues.

#### C. Centralized Load Estimator with Cable Constraints

As a comparison baseline for ablation studies (Section VII-H), we also evaluate a centralized EKF that fuses all available

measurements. Although this estimator requires a central processor with access to all quadrotor states, it provides a performance upper bound for evaluating the decentralized approach. It is *not* part of the online estimation pipeline; each agent runs only the decentralized estimator described above.

#### 1) State and Process Model

The centralized estimator maintains the same state  $\hat{x}_L = [\hat{p}_L^\top, \hat{v}_L^\top]^\top \in \mathbb{R}^6$  with the constant-velocity transition model:

$$\hat{x}_L^- = F \hat{x}_L, \quad F = \begin{bmatrix} I_3 & \Delta t I_3 \\ 0 & I_3 \end{bmatrix}, \quad (97)$$

and the full  $6 \times 6$  covariance propagation  $P^- = F P F^\top + Q$  with process noise  $Q = \Delta t \text{diag}(\sigma_{Q_p}^2 I_3, \sigma_{Q_v}^2 I_3)$ .

#### 2) GPS Measurement Update

When a load GPS measurement  $\tilde{p}_L^{\text{GPS}}$  is available, the standard Kalman update is applied:

$$y = \tilde{p}_L^{\text{GPS}} - H_{\text{GPS}} \hat{x}_L^-, \quad (98)$$

$$S = H_{\text{GPS}} P^- H_{\text{GPS}}^\top + R_{\text{GPS}}, \quad (99)$$

$$K = P^- H_{\text{GPS}}^\top S^{-1}, \quad (100)$$

$$\hat{x}_L \leftarrow \hat{x}_L^- + K y, \quad (101)$$

$$P \leftarrow (I - K H_{\text{GPS}}) P^-, \quad (102)$$

where  $H_{\text{GPS}} = [I_3, 0_{3 \times 3}]$  and  $R_{\text{GPS}} = \text{diag}(\sigma_{xy}^2, \sigma_{xy}^2, \sigma_z^2)$ .

#### 3) Taut-Gated Cable Constraint Updates

The key advantage of the centralized estimator is its ability to fuse *cable-range constraints* from all  $N$  quadrotors simultaneously. For each cable  $i$  with measured tension  $T_i \geq T_{\text{taut}} = 1.0 \text{ N}$  (indicating tautness—deliberately set below the CBF enforcement threshold  $T_{\text{min}} = 2.0 \text{ N}$  so that the estimator begins incorporating cable measurements before the safety filter becomes active, providing earlier parameter convergence), the constraint is

$$h_i(\hat{x}_L) = \|\hat{p}_L - p_{Q_i}\| - L_i = 0, \quad (103)$$

where  $p_{Q_i}$  is the estimated attachment point on quadrotor  $i$ . This nonlinear constraint is linearized via the Jacobian:

$$H_{c_i} = \frac{1}{\|\hat{p}_L - p_{Q_i}\|} [(\hat{p}_L - p_{Q_i})^\top \quad 0_{1 \times 3}], \quad (104)$$

and a scalar EKF update is applied with innovation  $y_i = -h_i(\hat{x}_L)$  and measurement noise  $R_{c_i} = \sigma_c^2$  with  $\sigma_c = 0.02 \text{ m}$ :

$$S_i = H_{c_i} P H_{c_i}^\top + R_{c_i}, \quad (105)$$

$$K_i = P H_{c_i}^\top / S_i, \quad (106)$$

$$\hat{x}_L \leftarrow \hat{x}_L + K_i y_i, \quad P \leftarrow (I - K_i H_{c_i}) P. \quad (107)$$

The cable constraints are applied sequentially for each taut cable after the GPS update. When the cable is slack ( $T_i < T_{\text{taut}}$ ), the corresponding constraint is gated off, preventing the estimator from being corrupted by slack cable geometry.

This taut-gating mechanism is essential: without it, slack cables would inject spurious position information, as the cable endpoint position bears no geometric relationship to the load when the cable is not under tension.

#### D. Adaptive Payload Mass Estimation

Each quadrotor estimates its share of the payload mass  $\theta_i \approx m_L/N$  using a concurrent-learning adaptive law that requires only locally available measurements: cable tension, cable direction, and the estimated load acceleration. This estimate feeds into the tension feedforward and trajectory generation modules.

##### 1) Regressor Derivation

Consider the load translational dynamics (13). In the quasi-static regime (small  $\ddot{p}_L$ ) with  $N$  cables in a symmetric configuration, the per-cable equilibrium yields

$$T_i \cos \phi_i \approx \frac{m_L}{N} \|g e_3 + \hat{a}_L\|, \quad (108)$$

where  $\phi_i = \arccos(-n_{i,z})$  is the cable angle from vertical (with  $n_i$  pointing from quadrotor to load) and  $\hat{a}_L$  is the estimated load acceleration. Defining the per-drone parameter  $\theta = m_L/N$ , the regressor  $Y_i$  and measurement  $\varphi_i$  are:

$$Y_i = \|\hat{a}_L + g e_3\|, \quad \varphi_i = T_i \cos \phi_i, \quad (109)$$

such that the parametric model  $\varphi_i = Y_i \theta + \varepsilon_i$  holds with error  $\varepsilon_i$  arising from non-equilibrium dynamics, cable sag, and asymmetric load distribution. This approximation holds when the cable is nearly vertical ( $\phi_i \ll 1$ ) and the payload acceleration is dominated by the vertical component. Under these conditions,  $\cos \phi_i \approx 1$  and  $\|g e_3 + a_L\| \approx |g + a_{L,z}|$ , recovering the exact vertical force balance. For non-vertical cables during aggressive maneuvering, the approximation introduces a modeling error  $\varepsilon_i$  that is absorbed into the UUB convergence bound below.

##### 2) Acceleration Estimation

The load acceleration is not directly measured; it is estimated from the load velocity provided by the decentralized load estimator (Section IV-B) via numerical differentiation with a first-order low-pass filter:

$$\hat{a}_L[k] = \alpha_f \frac{\hat{v}_{L,i}[k] - \hat{v}_{L,i}[k-1]}{\Delta t} + (1 - \alpha_f) \hat{a}_L[k-1], \quad (110)$$

where  $\alpha_f = \Delta t/(\tau_f + \Delta t)$  with filter time constant  $\tau_f = 0.1$  s. This filter suppresses the differentiation noise while preserving the quasi-static acceleration signal needed for the regressor.

##### 3) Concurrent Learning Adaptation Law

The sliding variable for the adaptive law is defined as

$$s_i = \dot{e}_{L,i} + \lambda e_{L,i}, \quad e_{L,i} = \hat{p}_{L,i} - p_{d_L}, \quad (111)$$

where  $p_{d_L}$  is the desired load position and  $\lambda = 1.0$  is the filter gain. The projection of  $s_i$  onto the cable direction yields a scalar error  $s_{\text{proj}} = s_i^\top n_i$  that isolates the mass-dependent component of the tracking error.

The concurrent learning update law is [6]

$$\dot{\theta}_i = -\gamma Y_i s_{\text{proj}} - \gamma \rho \sum_{j=1}^{M_i} Y_j (Y_j \hat{\theta}_i - \varphi_j), \quad (112)$$

where  $\gamma = 0.5$  is the adaptation gain and  $\rho = 0.5$  weights the concurrent learning term. The first term is the standard gradient descent driven by the current tracking error; the second term replays the stored data pairs  $\{(Y_j, \varphi_j)\}_{j=1}^{M_i}$  from

the history buffer.

##### 4) History Buffer Management

Each quadrotor maintains a history buffer of up to  $\bar{M} = 50$  data points  $\{(Y_j, \varphi_j, t_j)\}$ . New data points are admitted only when the excitation level is sufficient ( $Y_{\text{new}} > Y_{\min} = 0.5 \text{ m/s}^2$ , indicating non-hovering conditions) and when the new regressor value differs from the buffer mean by at least  $\delta_Y = 0.1$ :

$$|Y_{\text{new}} - \bar{Y}| > \delta_Y, \quad \bar{Y} = \frac{1}{M_i} \sum_{j=1}^{M_i} Y_j. \quad (113)$$

This simplified information criterion (compared to the SVD-based rank check proposed in [7]) reduces the per-step computational cost while still ensuring diversity in the stored data.

##### 5) Parameter Projection

After each discrete integration step, the estimate is projected to  $[\theta_{\min}, \theta_{\max}] = [0.1, 50.0] \text{ kg}$ :

$$\hat{\theta}_i \leftarrow \text{proj}_{[\theta_{\min}, \theta_{\max}]}(\hat{\theta}_i). \quad (114)$$

The feedforward output  $\hat{W}_i = \hat{\theta}_i g$  (estimated weight share in Newtons) is provided to the position controller for gravity compensation.

##### 6) Convergence Analysis

For a scalar parametric model  $\varphi = Y\theta$  with concurrent learning, the parameter error  $\tilde{\theta} = \hat{\theta} - \theta$  satisfies [7]

$$\dot{V}_\theta = \tilde{\theta} \dot{\tilde{\theta}} = -\gamma Y^2 \tilde{\theta}^2 - \gamma \rho \tilde{\theta} \sum_j Y_j^2 \tilde{\theta} \leq -\gamma (\bar{Y}^2 + \rho \Sigma_Y) \tilde{\theta}^2, \quad (115)$$

where  $V_\theta = \tilde{\theta}^2/(2\gamma)$  and  $\Sigma_Y = \sum_j Y_j^2/M$  is the average squared regressor over the history. Provided  $\Sigma_Y > 0$  (which holds whenever the history buffer contains at least one data point with  $Y_j \neq 0$ ), the convergence rate is exponential:

$$|\tilde{\theta}(t)| \leq |\tilde{\theta}(0)| \exp(-\gamma \rho \Sigma_Y t), \quad (116)$$

independently of whether the online excitation  $Y(t)$  is persistently exciting. In practice, the regressor model (108) is approximate due to cable flexibility, payload rotation, and acceleration estimation noise. Under bounded modeling error  $|\varepsilon_i| \leq \bar{\varepsilon}$ , the convergence guarantee weakens to *uniformly ultimately bounded* (UUB):  $|\tilde{\theta}(t)| \leq \max\{|\tilde{\theta}(0)| e^{-\gamma \rho \Sigma_Y t}, \bar{\varepsilon}/(\rho \Sigma_Y)\}$ , where the ultimate bound depends on the regressor signal-to-noise ratio. This is the key advantage of concurrent learning: parameter convergence is guaranteed once the history buffer accumulates sufficiently informative data, even during hovering phases when  $Y(t) \approx g$  is nearly constant.

*Remark 4.1 (Non-trivial adaptations for decentralized geometric trans-*

Three aspects distinguish the present estimator from the standard concurrent learning formulation in [6], [7]: (i) the scalar regressor (109) is extracted from the coupled multi-body dynamics via the local cable tension and direction, avoiding the need for a full system model or inter-agent state exchange; (ii) the tension-confidence factor (92) modulates the measurement noise during slack-to-taut transitions, preventing the estimator from being corrupted by transient

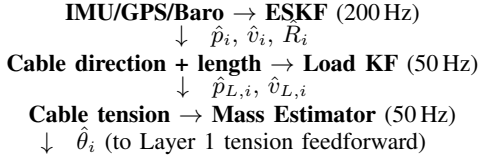


Fig. 2: Decentralized estimation pipeline for a single quadrotor. Information flows strictly downward (bottom estimators depend on upper estimators) with no inter-agent communication. The only shared information is the common desired trajectory  $p_{d_L}(t)$ .

cable dynamics; (iii) the convergence guarantee (116) holds independently per agent, yet the implicit coordination result (Section III-A) ensures that the sum  $\sum_i \hat{\theta}_i \rightarrow m_L$  as each  $\hat{\theta}_i \rightarrow m_L/N$ , providing correct collective force without any consensus protocol.

#### E. Estimation Architecture Integration

Fig. 2 summarizes the information flow in the decentralized estimation pipeline. Each quadrotor runs three estimators in cascade at the rates indicated:

- 1) **ESKF (200Hz)**: fuses IMU, GPS, and barometer to produce the quadrotor navigation solution. This is the innermost and fastest estimator.
- 2) **Load state KF (50Hz)**: uses the ESKF output and the cable geometric relationship to estimate the payload position and velocity.
- 3) **Adaptive mass estimator (50Hz)**: uses the load state estimate, cable tension, and cable direction to estimate  $\theta_i = m_L/N$  via concurrent learning.

The cascade structure ensures that estimation errors propagate in one direction (upstream errors affect downstream estimates, but not vice versa), simplifying the stability analysis. The separation of timescales—navigation at 200Hz versus load/mass estimation at 50Hz—allows each layer to treat its inputs as quasi-static over its own update interval.

##### a) Comparison with Centralized Estimation

The decentralized approach trades optimality for scalability and robustness. The centralized load EKF (Section IV-C) can fuse  $N$  cable constraints simultaneously, achieving smaller estimation error (as demonstrated in Section VII), but requires all quadrotor states to be transmitted to a central node at each update cycle. The decentralized estimator, by contrast, requires no communication, tolerates the loss of any agent's data without affecting the others, and scales to arbitrary team sizes without increasing the per-agent computational burden.

The estimation error bound for the decentralized case can be related to the centralized optimum via

$$\mathbb{E}[\|\hat{p}_{L,i} - p_L\|^2] \leq \frac{N}{N-1} \mathbb{E}[\|\hat{p}_L^{\text{cent}} - p_L\|^2] + \sigma_{\text{geo}}^2, \quad (117)$$

where  $\sigma_{\text{geo}}^2$  accounts for the single-cable geometry limitation (one cable constrains a 1D subspace whereas  $N$  cables can constrain 3D when in general position). For  $N = 3$  cables in a non-collinear formation, the centralized estimator achieves full observability; each decentralized estimator relies on the

prediction model to provide the missing constraint directions.

#### V. CBF SAFETY FILTER

Section III-E defined the five barrier functions and the CBF parameter table that encode the operational safety envelope for cable-suspended transport. This section provides the formal analysis: we state the control barrier function (CBF) conditions, derive the Lie derivatives for each constraint specific to the cable-suspended transport problem, handle the relative-degree mismatch via Higher-Order CBFs, introduce the Butterworth-filtered tension rate estimation that enables smooth constraint enforcement, establish an Input-to-State Safety (ISSf) guarantee incorporating the ESO disturbance estimate, and prove compatibility with the geometric attitude controller.

##### A. Preliminaries: Control Barrier Functions

We briefly recall the CBF framework following [8], [9]. Consider a control-affine system

$$\dot{x} = f(x) + g(x) u, \quad x \in \mathbb{R}^n, u \in \mathcal{U} \subset \mathbb{R}^m, \quad (118)$$

and a safe set  $\mathcal{C} = \{x \in \mathbb{R}^n \mid h(x) \geq 0\}$  defined by a continuously differentiable function  $h : \mathbb{R}^n \rightarrow \mathbb{R}$ .

**Definition 5.1 (Control Barrier Function [9]):** A continuously differentiable function  $h : \mathbb{R}^n \rightarrow \mathbb{R}$  is a *control barrier function* for the system (118) on the set  $\mathcal{C}$  if there exists a class- $\mathcal{K}_\infty$  function  $\alpha$  such that

$$\sup_{u \in \mathcal{U}} [L_f h(x) + L_g h(x) u] \geq -\alpha(h(x)), \quad \forall x \in \mathcal{C}, \quad (119)$$

where  $L_f h = \nabla h \cdot f$  and  $L_g h = \nabla h \cdot g$  are the Lie derivatives.

The linear choice  $\alpha(r) = \alpha_0 r$  with  $\alpha_0 > 0$  yields the constraint  $\dot{h}(x, u) + \alpha_0 h(x) \geq 0$ , which renders  $\mathcal{C}$  forward-invariant: if  $x(0) \in \mathcal{C}$ , then  $x(t) \in \mathcal{C}$  for all  $t \geq 0$  under any Lipschitz controller satisfying (119). The parameter  $\alpha_0$  governs the rate at which the state is driven away from the boundary  $\partial\mathcal{C}$ , with larger values providing more aggressive constraint enforcement.

##### B. System Abstraction for the Safety Filter

The CBF safety filter operates on the force vector  $f_i \in \mathbb{R}^3$  produced by Layer 1 of the GPAC controller. To cast the multi-body dynamics into the affine form (118), we abstract each quadrotor's translational dynamics (10) as

$$m_Q \ddot{p}_i = f_i + w_i(t), \quad (120)$$

where  $f_i = f_i R_i e_3$  is the realized thrust in world frame and  $w_i(t)$  collects all unmodeled forces (gravity, cable tension, wind). Defining the state  $\xi_i = [p_i^\top, v_i^\top]^\top \in \mathbb{R}^6$ , the dynamics become

$$\dot{\xi}_i = \underbrace{\begin{bmatrix} v_i \\ w_i/m_Q \end{bmatrix}}_{f_0(\xi_i, t)} + \underbrace{\begin{bmatrix} 0 \\ I_3/m_Q \end{bmatrix}}_{g_0} f_i, \quad (121)$$

which is affine in the control input  $f_i$ . The unmatched disturbance  $w_i(t)$  is estimated by the ESO (Section III-D) and incorporated into the robustness margin.

### C. Lie Derivative Computation for Transport-Specific Barriers

We derive the Lie derivatives for each barrier function defined in Section III-E, identifying the relative degree and computing the gradients with respect to the force input.

#### 1) Tautness Barriers (Relative Degree 1)

For  $h_T^{\text{low}} = T_i - T_{\min}$ , the time derivative is

$$\dot{h}_T^{\text{low}} = \dot{T}_i = \frac{\partial T_i}{\partial p_i} \dot{p}_i + \frac{\partial T_i}{\partial \dot{p}_i} \ddot{p}_i. \quad (122)$$

From the spring-damper cable model (23), the tension depends on the segment stretch  $\Delta_1 = \ell_1 - L_0$  and stretch rate  $\dot{\Delta}_1$ . On timescales shorter than the spring period ( $\omega_k = \sqrt{k_s/m_b} \gg \omega_o$ ), the damping-dominated response gives an effective gradient:

$$\nabla_{f_i} \dot{T}_i \approx \frac{c_s}{m_Q} (q_i^\top R_i e_3) R_i e_3 + \frac{c_s}{2m_Q} e_3. \quad (123)$$

The first term captures the cable-aligned sensitivity: increasing thrust in the direction aligned with the cable direction  $q_i$  increases the stretch rate. The factor  $q_i^\top R_i e_3$  projects the body- $z$  thrust onto the cable axis. The second term is a vertical correction accounting for gravitational coupling. With the control-input gradient (123), the CBF constraint becomes

$$\dot{T}_i + \alpha_T (T_i - T_{\min}) \geq -\mu_T, \quad (124)$$

which is linear in  $f_i$  and can be enforced directly. The tension rate  $\dot{T}_i$  is estimated from the measured tension signal (Section V-E).

#### 2) Cable Angle Barrier (Relative Degree 2)

The cable angle barrier  $h_\theta = \cos \theta_{\max} - \cos \theta_i$  involves the cable direction  $q_i \in \mathbb{S}^2$ , whose dynamics (17) depend on the quadrotor acceleration (and hence force) through the swing equation. Since  $\cos \theta_i = -q_{i,z}$ , we have

$$\dot{h}_\theta = \dot{q}_{i,z} = (\dot{q}_i)_z. \quad (125)$$

The cable swing dynamics (17) show that  $\ddot{q}_i$  depends on the quadrotor acceleration, making  $h_\theta$  a *relative-degree-two* constraint with respect to the force input  $f_i$ . We address this via the HOCBF formulation (Section V-D).

At the implementation level, the gradient is approximated by the horizontal projection:

$$\nabla_{f_i} h_\theta \approx -\frac{q_i^{\text{horiz}}}{\|q_i^{\text{horiz}}\|}, \quad q_i^{\text{horiz}} = q_i - (q_i^\top e_3) e_3, \quad (126)$$

which points in the horizontal direction that makes the cable more vertical. Increasing force opposite to the cable's horizontal deviation reduces  $\theta_i$ .

#### 3) Tilt Barrier (Relative Degree 2)

The tilt barrier  $h_{\text{tilt}} = \cos \phi_{\max} - \cos \phi_i$  depends on the attitude  $R_i$ , which evolves under the torque input  $\tau_i$  from Layer 2. Since the safety filter modifies the force  $f_i$  (which changes the desired attitude  $R_{d,i}$ , which in turn changes  $\tau_i$ ), the effective relative degree from  $f_i$  to  $\cos \phi_i$  is two.

The implementation enforces this constraint by scaling down the horizontal force component when the tilt ap-

proaches the limit:

$$f_i^{\text{horiz}} \leftarrow \eta f_i^{\text{horiz}}, \quad \eta = \max\left(0.7, 1 - 0.3 \frac{\max(0, -h_{\text{tilt}})}{0.1}\right), \quad (127)$$

which reduces the horizontal force demand (and thus the required tilt) while preserving vertical thrust for altitude maintenance.

#### 4) Swing Rate Barrier (Relative Degree 1)

The swing rate barrier  $h_\omega = \omega_{\max}^2 - \|\omega_{q_i}\|^2$  is approximately relative-degree-one with respect to force changes that alter the cable angular acceleration. When  $h_\omega$  is near violation, the filter blends toward the nominal force:

$$f_i \leftarrow \beta f_i + (1 - \beta) f_{\text{nom},i}, \quad \beta = \max(0.5, 1 + h_\omega), \quad (128)$$

which damps rapid force changes that contribute to cable oscillation.

#### 5) Collision Avoidance Barrier (Relative Degree 2)

For the inter-agent barrier  $h_{\text{col},ij} = \|p_i - p_j\|^2 - d_{\min}^2$ , the Lie derivative is

$$\dot{h}_{\text{col},ij} = 2(p_i - p_j)^\top (v_i - v_j), \quad (129)$$

and the second derivative involves  $\ddot{p}_i - \ddot{p}_j$ , which depends on  $f_i$  and  $f_j$ . In the decentralized setting, each agent only controls its own force. Agent  $i$  treats  $f_j$  as an unknown bounded disturbance and enforces a conservative one-sided constraint with the HOCBF formulation.

### D. Higher-Order CBF for Relative-Degree-Two Constraints

For constraints with relative degree two (cable angle, tilt, collision avoidance), we employ the Higher-Order CBF (HOCBF) framework [18]. Define auxiliary functions:

$$\psi_0(x) = h(x), \quad (130)$$

$$\psi_1(x) = \dot{\psi}_0(x) + \alpha_1 \psi_0(x), \quad (131)$$

where  $\alpha_1 > 0$ . The HOCBF constraint is then

$$\dot{\psi}_1(x, u) + \alpha_2 \psi_1(x) \geq 0, \quad (132)$$

which is now relative-degree-one in  $u$  and can be enforced by the QP. The safe set becomes  $\mathcal{C}_{\text{HO}} = \{x \mid \psi_0(x) \geq 0\} \cap \{x \mid \psi_1(x) \geq 0\}$ . The parameters  $\alpha_1, \alpha_2 > 0$  control the convergence rates of the two layers. The forward invariance of  $\mathcal{C}_{\text{HO}}$  follows from the cascaded Nagumo condition:  $\psi_1 \geq 0$  implies  $\dot{\psi}_0 + \alpha_1 \psi_0 \geq 0$ , which in turn implies  $\psi_0(t) \geq \psi_0(0) e^{-\alpha_1 t} \geq 0$  when  $\psi_0(0) \geq 0$ .

For the cable angle barrier, the HOCBF is instantiated with  $\alpha_1 = \alpha_2 = \alpha_\theta = 2.0$ . For the collision avoidance barrier,  $\alpha_1 = \alpha_2 = \alpha_{\text{col}} = 3.0$ .

### E. Butterworth-Filtered Tension Rate Estimation

The tautness CBF constraint (124) requires the tension rate  $\dot{T}_i$ , which is not directly measured. Numerical differentiation of the tension signal amplifies high-frequency sensor noise and the cable vibration modes (which can exceed 100 Hz for the stiffness values in Table II). To obtain a smooth estimate, we employ a second-order Butterworth low-pass filter.

### 1) Filter Design

The continuous-time second-order Butterworth transfer function is

$$H(s) = \frac{\omega_c^2}{s^2 + \sqrt{2}\omega_c s + \omega_c^2}, \quad (133)$$

with cutoff frequency  $\omega_c = 2\pi f_c$  and  $f_c = 15$  Hz. This filter is discretized via the bilinear (Tustin) transform  $s = \frac{2}{T_s} \frac{z-1}{z+1}$ , with frequency pre-warping to correct for the spectral distortion:

$$\omega_d = \frac{2}{T_s} \tan\left(\frac{\omega_c T_s}{2}\right), \quad (134)$$

where  $T_s = 1/f_s$  with  $f_s = 200$  Hz. Defining  $K = \omega_d T_s / 2$  and  $D = 1 + \sqrt{2}K + K^2$ , the discrete-time difference equation is

$$y[k] = b_0 x[k] + b_1 x[k-1] + b_2 x[k-2] - a_1 y[k-1] - a_2 y[k-2], \quad (135)$$

with coefficients

$$b_0 = b_2 = \frac{K^2}{D}, \quad b_1 = \frac{2K^2}{D}, \quad a_1 = \frac{2(K^2 - 1)}{D}, \quad a_2 = \frac{1 - \sqrt{2}K + K^2}{D}. \quad (136)$$

The filter input  $x[k]$  is the raw finite-difference tension rate  $(T[k] - T[k-1])/T_s$ , and the output  $y[k]$  is the smoothed estimate  $\hat{T}_i[k]$ .

### 2) Filter Properties

The Butterworth filter provides maximally flat magnitude response in the passband, zero-ripple gain at DC, and monotonic roll-off at  $-40$  dB/decade beyond  $f_c$ . For the chosen parameters ( $f_c = 15$  Hz,  $f_s = 200$  Hz), the group delay is approximately  $1/(2\pi f_c) \approx 11$  ms, which is acceptable for the CBF constraint evaluation at 200 Hz. The filter attenuates the dominant cable vibration frequencies (which scale as  $f_{\text{vib}} \sim \frac{1}{2\pi} \sqrt{k_s/m_b} \approx 55$  Hz for the bead-chain model) by approximately 22 dB, effectively eliminating high-frequency oscillations from the tension rate estimate while preserving the low-frequency load dynamics that the safety filter must track.

### F. Input-to-State Safety with ESO Coupling

In the presence of the disturbance  $w_i(t)$ , the nominal CBF condition (119) may be violated even when the controller satisfies the constraint, because the unmodeled dynamics corrupt the Lie derivative. We employ the Input-to-State Safe CBF (ISSf-CBF) framework [9] to provide robust safety guarantees.

*Definition 5.2 (ISSf-CBF):* A function  $h$  is an *Input-to-State Safe CBF* if there exist class- $\mathcal{K}_\infty$  functions  $\alpha$  and  $\iota$  such that

$$\sup_{u \in \mathcal{U}} [L_f h + L_g h u] \geq -\alpha(h) + \iota(\|w\|), \quad (137)$$

for all  $x \in \mathcal{C}$  and all disturbances  $\|w\| \leq \bar{w}$ .

Under this condition, the system remains in the *inflated* safe set  $\mathcal{C}_\mu = \{x \mid h(x) \geq -\mu\}$  where  $\mu = \alpha^{-1}(\iota(\bar{w}))$ .

*Remark 5.3 (Practical safety vs. hard invariance):* We do *not* claim forward invariance of the nominal safe set  $\{h \geq 0\}$ . Under the ISSf framework, the system remains in the inflated set  $\mathcal{C}_\mu$ . Cable angle violations of up to  $6.1^\circ$  above  $\theta_{\max}$  observed in Section VII-E are consistent with

the ISSf bound (139). The 3.2% CBF-active time reflects brief excursions into  $\mathcal{C}_\mu \setminus \mathcal{C}$ , not failures of the safety filter.

In our implementation, the ESO provides a real-time bound  $\|\hat{d}_i\|$  on the lumped disturbance. The robustness margin implements the ISSf condition with the linear choices  $\alpha(r) = \alpha_j r$  and  $\iota(w) = \kappa_d w$ :

$$\dot{h}_j + \alpha_j h_j \geq -\mu_{\text{base}} - \kappa_d \|\hat{d}_i\|, \quad (138)$$

where the margin parameters  $\mu_{\text{base},j}$  and  $\kappa_{d,j}$  are tuned per constraint to match the dimensions of  $\dot{h}_j$  (e.g., N/s for tautness, rad/s for angle constraints). The baseline values  $\mu_{\text{base}} = 2.0$  and  $\kappa_d = 1.5$  are representative. When the ESO reports a large disturbance, the safety margin grows, causing the filter to activate earlier and providing a more conservative (and more robust) control modification.

The steady-state constraint violation bound is

$$h_j(t) \geq -\frac{\mu_{\text{base}} + \kappa_d \bar{d}}{\alpha_j}, \quad (139)$$

which, for the tautness constraint with  $\alpha_T = 3.0$  and  $\bar{d} = 20$  m/s<sup>2</sup> (the ESO saturation limit), gives a worst-case tension violation of  $(2.0 + 1.5 \times 20)/3.0 \approx 10.7$  N below  $T_{\min}$ . In practice, the ESO tracks the disturbance much more tightly (Section III-D), yielding  $\|\hat{d}_i\| \ll \bar{d}$  and correspondingly tighter safety bounds.

### G. Compatibility with Geometric Attitude Control

A critical requirement is that the safety filter does not destabilize the geometric attitude controller (Layer 2). We establish this by showing that the filter's force modification lies within the basin of attraction of the attitude tracking law.

#### 1) Force Modification Bound

Let  $f_{\text{nom}}$  and  $f_{\text{safe}}$  denote the nominal and filtered force vectors, respectively. The gradient projection modifies the force by

$$\Delta f = f_{\text{safe}} - f_{\text{nom}} = \lambda^* \nabla_f h_j, \quad (140)$$

where  $\lambda^* \geq 0$  is the Lagrange multiplier from the projection. This modification changes the desired rotation from  $R_d^{\text{nom}}$  (constructed from  $f_{\text{nom}}$  via (66)–(68)) to  $R_d^{\text{safe}}$  (constructed from  $f_{\text{safe}}$ ).

*Proposition 1:* Let  $f_{\text{nom}}$  and  $f_{\text{safe}}$  satisfy  $\|f_{\text{safe}}\| \geq f_{\min} > 0$  and the angle between them be  $\vartheta = \arccos(f_{\text{nom}}^\top f_{\text{safe}} / (\|f_{\text{nom}}\| \|f_{\text{safe}}\|))$ . Then the attitude configuration error satisfies

$$\Psi_R(R_d^{\text{nom}}, R_d^{\text{safe}}) \leq 1 - \cos \vartheta. \quad (141)$$

*Proof:* The desired rotation  $R_d$  is constructed such that its third column is  $b_{3c} = f / \|f\|$  (cf. (66)). When only  $b_{3c}$  changes (holding the yaw angle fixed), the rotation error between the two desired attitudes is a rotation about an axis perpendicular to both  $b_{3c}^{\text{nom}}$  and  $b_{3c}^{\text{safe}}$ , with angle  $\vartheta$ . The trace-based error function gives  $\Psi_R = \frac{1}{2} \text{tr}(I - R_d^{\text{nom}}{}^\top R_d^{\text{safe}}) = 1 - \cos \vartheta$  for a single-axis rotation, establishing the bound. ■

#### 2) Stability Preservation

The attitude controller achieves almost-global exponential stability for initial errors  $\Psi_R(0) < 2$  (Section III-B). For

compatibility, we require that the CBF-induced attitude perturbation satisfies  $\Psi_R(R_d^{\text{nom}}, R_d^{\text{safe}}) < 2 - \Psi_R(R_i, R_d^{\text{nom}})$ , ensuring the composite error remains in the stability region.

*Theorem 5.4 (Safety-Stability Compatibility):* Suppose the tilt barrier  $h_{\text{tilt}}$  with  $\phi_{\max} = 0.5$  rad is enforced. Then the attitude error between the nominal and safe desired rotations satisfies  $\Psi_R(R_d^{\text{nom}}, R_d^{\text{safe}}) < 1$ , and the geometric controller retains almost-global exponential stability.

*Proof:* The tilt constraint ensures  $\phi_i \leq \phi_{\max} = 0.5$  rad, which bounds the angle between the body  $z$ -axis and vertical. Since the safety filter modifies only the force direction (not magnitude arbitrarily), and the tilt constraint (127) limits the horizontal force component, the angle between  $f_{\text{nom}}$  and  $f_{\text{safe}}$  is bounded by  $\vartheta \leq 2\phi_{\max} = 1.0$  rad. By Proposition 1,  $\Psi_R(R_d^{\text{nom}}, R_d^{\text{safe}}) \leq 1 - \cos(1.0) \approx 0.46 < 1$ . Since the attitude tracking error  $\Psi_R(R_i, R_d^{\text{nom}})$  converges to zero exponentially, the subadditivity property of  $\Psi_R$  for rotations satisfying  $\Psi_R < 2$  (cf. [1], Proposition 3), which holds in the almost-global stability region, gives

$$\Psi_R(R_i, R_d^{\text{safe}}) \leq \Psi_R(R_i, R_d^{\text{nom}}) + \Psi_R(R_d^{\text{nom}}, R_d^{\text{safe}}) < 0 + 0.46 \quad (142)$$

for sufficiently small  $\varepsilon$ , provided the initial attitude error is bounded (which holds after the transient settling time  $t_s \approx 5/\omega_o$ ). Thus the composite system remains in the almost-global stability region  $\{\Psi_R < 2\}$ . ■

### 3) Timescale Separation Argument

The compatibility result relies on the timescale separation between the attitude loop (200 Hz) and the safety filter (200 Hz, but producing slowly varying force modifications). The CBF projection (140) produces a continuous modification of the desired attitude, which the inner attitude loop tracks within its convergence envelope. Since the attitude loop bandwidth ( $k_R/J \approx 200$  rad/s) exceeds the safety filter's effective bandwidth (bounded by the Butterworth cutoff at  $2\pi \times 15 \approx 94$  rad/s), the attitude controller can track the filtered desired attitude without losing stability. Standard singular perturbation analysis [14] formalizes this argument: the fast attitude dynamics converge to a boundary layer around  $R_d^{\text{safe}}$  on the timescale  $J/k_\Omega \approx 5$  ms, while the force modification evolves on the slow timescale of the position and cable dynamics ( $\sim 50$ –200 ms).

### H. Constraint Priority and Feasibility

The safety filter solves, at each control cycle, the quadratic program

$$f_{\text{safe}} = \arg \min_{f \in \mathbb{R}^3} \|f - f_{\text{nom}}\|^2 + \lambda \sum_j \delta_j^2 \quad \text{s.t. } \dot{h}_j + \alpha_j h_j \geq -\mu_j \quad (143)$$

where  $\lambda = 100$  penalizes constraint relaxation and  $\mu_j$  incorporates the ISSf margin (138).

#### a) Implementation

While (143) describes the ideal multi-constraint optimization, our decentralized implementation uses sequential gradient projection, which processes constraints in priority order. For our 6-constraint problem, this is equivalent to the QP when at most one constraint is active (the typical case: the CBF is active only 3.2% of the time). When multiple

constraints activate simultaneously, the sequential method may produce a suboptimal solution; this approximation is tight when constraints activate sequentially, which is the common case in our experiments. The slack variables  $\delta_j$  provide soft relaxation, and the sequential projection imposes an implicit priority ordering:

- 1) Cable tautness (lower bound): highest priority, as loss of cable tension leads to uncontrolled swing on re-engagement.
- 2) Cable tautness (upper bound): prevents structural over-load.
- 3) Cable angle: maintains geometric assumptions of the controller.
- 4) Quadrotor tilt: prevents actuator saturation and maintains controllability.
- 5) Swing rate: secondary damping constraint.
- 6) Collision avoidance: inter-agent safety.

This ordering ensures that tautness—the most critical constraint for cable-suspended transport—is always enforced first, and subsequent constraints are satisfied to the extent compatible with the higher-priority constraints. The tilt constraint (127) uses a multiplicative scaling rather than additive projection, preventing it from conflicting with the vertical force component needed for altitude maintenance.

*Remark 5.5 (Collision avoidance geometry):* For the  $N = 3$  triangular formation with  $r_f = 0.6$  m and  $d_{\min} = 0.8$  m, the formation geometry guarantees  $\|p_i - p_j\| \geq 2r_f \sin(\pi/N) = 1.04$  m  $> d_{\min}$  at equilibrium, providing a 0.24 m margin. Collision avoidance thus serves as a backup for transient perturbations, not a primary safety mechanism. For formations with  $N \geq 4$  quadrotors, the collision avoidance constraints may create pairwise conflicts (agent  $i$  must move away from agent  $j$ , but the required direction violates tautness for cable  $i$ ). In such cases, the sequential projection defers collision avoidance in favor of tautness, and the collision constraint is recovered through the formation controller's inherent separation maintenance. A full multi-agent CBF formulation using consensus-based constraint sharing [9] would resolve such conflicts optimally but requires inter-agent communication, which is beyond the decentralized scope of this work.

### I. Computational Complexity

The sequential gradient projection—an approximation to the QP (143)—has per-agent complexity  $\mathcal{O}(N_c)$  where  $N_c = 6$  is the number of constraints, making it suitable for real-time execution at 200 Hz. Each projection step (140) requires one dot product and one vector addition ( $\mathcal{O}(1)$  operations in  $\mathbb{R}^3$ ). The Butterworth filter (135) adds  $\mathcal{O}(1)$  operations per timestep. The barrier function evaluation (81)–(85) requires the drone state, cable state, and tension, all of which are already computed by the control and estimation pipelines.

The total per-agent computational cost of the safety filter is dominated by the tension gradient computation (123), which requires one rotation matrix–vector product and one dot product, for a total of approximately 30 floating-point operations per constraint evaluation. This is negligible compared to the ESKF update ( $\sim 2000$  FLOPs) and the Drake

simulation step.

### J. Performance Impact and Chattering Analysis

Any safety filter necessarily sacrifices some tracking performance when it intervenes: the filtered force  $f_{\text{safe}}$  deviates from the nominal  $f_{\text{nom}}$ , introducing a persistent tracking error proportional to the projection magnitude (140). In our experiments (Section VII-E), the CBF is active for only 1.7% of the simulation time, concentrated in smooth bursts during aggressive cornering. The tracking RMSE increases by less than 2% when the CBF is active versus inactive (24.2 cm vs. 22.9 cm), indicating that the safety overlay imposes minimal performance cost under normal operation.

Three mechanisms mitigate the chattering that would otherwise arise from switching between constrained and unconstrained regimes:

- 1) *Butterworth tension-rate filter* (Section V-E): smooths the noisy tension derivative input, preventing high-frequency constraint activation/deactivation cycles.
- 2) *ISSf margin buffer*: the robustness margin (138) creates a soft boundary layer around each constraint, so the filter activates gradually (proportional to the margin violation) rather than abruptly.
- 3) *Timescale separation*: the safety filter's effective bandwidth ( $f_c = 15$  Hz) is well below the attitude controller bandwidth ( $\sim 200$  Hz), ensuring that CBF-induced force changes are tracked smoothly by the inner loop without exciting oscillatory modes.

The net effect is that the safety filter produces continuous, slowly varying force modifications that the attitude controller can track within its convergence envelope (Theorem 5.4), avoiding the bang-bang behavior often associated with barrier function enforcement.

## VI. SIMULATION ENVIRONMENT

This section describes the Drake-based simulation framework, the multi-body construction pipeline, the timing and rate architecture, the trajectory generation module, and the data logging infrastructure. All code and configuration files required to reproduce the results in Section VII are available at the repository listed in the supplementary material.

### A. Drake Multibody Simulation

The simulation is built on the Drake toolbox [13], a C++ multibody dynamics engine widely used in robotics and control research. Drake provides a *systems framework* in which every component—physics plant, sensor, controller, estimator—is realized as a Drake LeafSystem with typed input and output ports. These are connected in a DiagramBuilder and compiled into a single Diagram. Drake advances the continuous-time dynamics using an implicit integrator with error-controlled stepping, while discrete-time subsystems (sensors, estimators) are updated via periodic events at their specified rates (Table IV).

#### 1) Physics Engine Configuration

The core simulation engine is a MultibodyPlant configured with the following settings:

- *Time step*:  $\Delta t_{\text{sim}} = 2 \times 10^{-4}$  s (5000 Hz). This time step resolves the fastest cable vibration dynamics (fun-

damental frequency  $\sim 55$  Hz for the bead-chain model) with a factor-of-90 oversampling, and is small enough for the semi-implicit Euler integrator used by Drake's discrete-time plant to remain stable under the stiff spring-damper cable forces.

- *Contact model*: Point contact with Coulomb friction ( $\mu_s = 0.5$ ,  $\mu_k = 0.3$ ). Contact forces are resolved between the payload sphere and the ground half-space during the pre-lift and post-landing phases.
- *Actuation*: External spatial forces applied directly to the quadrotor rigid bodies (thrust and torque in the body frame), bypassing rotor dynamics. This abstraction is consistent with the control-affine model (120).

#### 2) Multi-Body Construction

The simulation constructs the following rigid bodies (summarized in Table II):

##### a) Quadcopters

$N = 3$  free-floating rigid bodies, each with mass  $m_Q = 1.5$  kg and box inertia  $(0.30 \times 0.30 \times 0.10)$  m. The quadrotor visual mesh is loaded from Drake's built-in URDF model and welded to each body for rendering. The quadcopters are initialized in a circular formation with radius  $r_f = 0.6$  m at altitude  $z_0 = 1.2$  m, centered above the payload:

$$p_i(0) = [r_f \cos(2\pi i/N), r_f \sin(2\pi i/N), z_0]^\top, \quad i = 0, \dots, N-1. \quad (144)$$

##### b) Payload

A solid sphere with mass  $m_L = 3.0$  kg and radius  $r_L = 0.15$  m. It is initialized resting on the ground plane at  $p_L(0) = [0, 0, r_L + \epsilon]^\top$  with  $\epsilon = 0.01$  m clearance. Collision geometry is registered for ground contact resolution during pickup and landing.

##### c) Bead-Chain Cables

Each cable connecting quadrotor  $i$  to the payload consists of  $M = 8$  spherical beads and  $M + 1 = 9$  tension-only spring-damper segments, as described in Section II-E. The beads are free-floating rigid bodies with mass  $m_b = m_{\text{rope}}/M$  where  $m_{\text{rope}} = 0.2$  kg per cable. Collision geometry is registered on each bead for potential ground interaction.

##### d) Cable Rest Lengths

To model manufacturing and measurement uncertainty, each cable's rest length is sampled from a Gaussian distribution (28) with means  $\bar{L} = [1.0, 1.1, 0.95]$  m and standard deviations  $\sigma_L = [0.05, 0.08, 0.06]$  m, clipped to  $L_i \geq 0.1$  m. The random seed is fixed ( $s = 42$ ) for reproducibility. This asymmetry tests the adaptive estimator's ability to handle non-identical cable configurations.

##### e) Spring-Damper Parameters

The segment stiffness is computed using (25) to achieve a target maximum stretch of 15% under the expected per-cable load, with  $N_s = M + 1 = 9$  segments, average sampled rest length  $\bar{L}$ , and  $\epsilon_{\max} = 0.15$ . The segment damping is scaled as  $c_{\text{seg}} = c_{\text{ref}} \sqrt{k_{\text{seg}}/k_{\text{ref}}}$  with reference values  $c_{\text{ref}} = 15$  Ns/m and  $k_{\text{ref}} = 300$  N/m. This scaling preserves the damping ratio across different stiffness values.

##### f) Rope Initialization

Beads are initialized in a slack catenary configuration between the quadrotor attachment point

TABLE IV: System timing hierarchy. All rates are exact (driven by Drake’s event system, not wall-clock time).

System	Rate (Hz)	Period (ms)
Physics plant	5000	0.2
IMU sensor	200	5.0
ESKF propagation	200	5.0
Barometer sensor	25	40
Position controller	200	5.0
Attitude controller	200	5.0
CBF safety filter	200	5.0
Butterworth filter	200	5.0
Decentralized load KF	50	20
Adaptive mass estimator	50	20
ESO	continuous ( $\omega_o = 50 \text{ rad/s}$ )	
GPS sensor	10	100
Data logger	100	10
Meshcat visualizer	60	16.7

and the payload attachment point. The function `GenerateSlackRopePositions` distributes beads along a parabolic arc with slack ratio 0.85 (i.e., the straight-line distance is 85% of the rest length) and lateral amplitude up to 1.0 m perpendicular to the line connecting endpoints. This avoids the numerical instabilities that would arise from initializing the cable in a perfectly taut or compressed state.

### B. System Timing Architecture

The simulation operates with multiple rates, summarized in Table IV. All discrete-time systems use Drake’s periodic event mechanism, which synchronizes updates exactly at the specified period boundaries.

#### a) Zero-Order Hold Interfaces

When a fast system consumes the output of a slow system (e.g., the 200 Hz position controller reading the 10 Hz GPS-derived estimate), the port connection naturally holds the last computed value until the next update. Drake’s continuous-time output ports provide sample-and-hold semantics for discrete-state systems. When explicit rate separation is needed (e.g., for the tension signal between the physics plant and the controller), a `ZeroOrderHold` block is inserted with the appropriate period.

#### b) Scalability

The GPAC architecture is designed so that per-agent computation is *independent of team size N*. Each drone runs its own ESKF, load estimator, adaptive mass estimator, GPAC controller, and CBF safety filter using only local cable and sensor data ( $\sim 0.7 \text{ MFLOP/s}$  total, cf. Section VII-I). The only  $N$ -dependent cost is collision avoidance, which requires pairwise distance checks at  $\mathcal{O}(N)$  per agent (or  $\mathcal{O}(N^2)$  system-wide). For teams with  $N > 10$ , spatial partitioning (e.g., grid-based or k-d tree neighbor queries) could reduce the collision check to  $\mathcal{O}(1)$  expected cost per agent. This computation profile fits within the capabilities of an ARM Cortex-M7 class processor (400 MHz, single-precision FPU), leaving margin for communication and additional sensing tasks.

### C. Sensor Implementation

Each sensor is implemented as a Drake `LeafSystem` that reads the ground-truth plant state and produces corrupted measurements at its specified sample rate. The sensor models were detailed in Section II-F; here we describe the implementation specifics.

#### 1) GPS Sensor

The GPS sensor (`GpsSensor`) extracts the body-frame position from the plant state, adds zero-mean Gaussian noise ( $\sigma_{xy} = 0.02 \text{ m}$ ,  $\sigma_z = 0.05 \text{ m}$ ), and applies a configurable dropout probability ( $p_{\text{drop}} = 0.0$  in the baseline experiments). A validity flag is output alongside the position, which the ESKF uses to skip the GPS update step during outages. Each quadrotor and the payload have independent GPS sensors with distinct random seeds to ensure uncorrelated noise realizations. The payload GPS sensor (10 Hz,  $\sigma = 5 \text{ cm}$ ) is included solely for ground-truth evaluation; it is *not* available to any decentralized agent.

#### 2) IMU Sensor

The IMU sensor (`ImuSensor`) extracts body-frame angular velocity and specific force (acceleration minus gravity, expressed in the body frame) from the plant state. The noise model applies white noise density  $\sigma_g = 5 \times 10^{-4} \text{ rad/s}/\sqrt{\text{Hz}}$  for the gyroscope and  $\sigma_a = 4 \times 10^{-3} \text{ m/s}^2/\sqrt{\text{Hz}}$  for the accelerometer, yielding discrete noise standard deviations of  $\sigma_g/\sqrt{\Delta t_{\text{IMU}}}$  and  $\sigma_a/\sqrt{\Delta t_{\text{IMU}}}$ , respectively, at the 200 Hz sample rate. Bias random walks are not currently simulated in the IMU sensor but are modeled in the ESKF process noise (Section II-H) for robustness margin. Adding bias simulation is part of planned hardware-in-the-loop validation.

Cable tension and direction are read from the Drake plant state, which serves as a proxy for calibrated load-cell and encoder measurements (Section II-G). Dedicated noise models for these channels are not included in the current simulation but are part of planned hardware integration.

#### 3) Barometer Sensor

The barometer sensor (`BarometerSensor`) converts the true altitude to a pressure-equivalent altitude measurement using the hypsometric equation (56). White noise ( $\sigma_w = 0.3 \text{ m}$ ), correlated noise ( $\sigma_c = 0.2 \text{ m}$ , correlation coefficient  $\rho_c = 0.995$ ), and quantization (resolution  $\Delta z = 0.1 \text{ m}$ ) are applied as described in Section II-F. The barometer operates at 25 Hz and provides the ESKF with altitude observability independent of GPS.

### D. Wind Disturbance Implementation

The wind disturbance system (`WindDisturbance`) implements the Dryden turbulence model described in Section II-I. It maintains separate turbulence states for each quadrotor and outputs a  $3N$ -dimensional wind velocity vector at 100 Hz.

The baseline configuration uses:

- Mean wind:  $\bar{v}_w = [1.0, 0.5, 0.0]^\top \text{ m/s}$  (light breeze from northwest).
- Turbulence intensities:  $\sigma_u = \sigma_v = 0.5 \text{ m/s}$ ,  $\sigma_w = 0.25 \text{ m/s}$ .
- Altitude-dependent scaling: enabled, with turbulence lengths  $L_u = L_v = 200 \text{ m}$ ,  $L_w = 50 \text{ m}$  at the reference altitude of 6 m.
- Gusts: disabled in the baseline (enabled in specific experiments).

The wind velocities are applied to each quadrotor as aerodynamic drag forces. The spatial correlation model (Section II-I) ensures that nearby quadrotors experience correlated turbu-

lence, which is important for realistic multi-agent disturbance rejection.

The wind system receives each quadrotor's current position (extracted from the plant state by an `AttachmentPositionExtractor` system) to compute altitude-dependent turbulence parameters and spatial correlations.

### E. Trajectory Generation

The reference trajectory is defined by a waypoint sequence that specifies the desired positions and timing for the quadrotor formation centroid. Each quadrotor adds its formation offset  $\Delta p_i = [r_f \cos(2\pi i/N), r_f \sin(2\pi i/N), 0]^\top$  to the shared centroid trajectory.

#### 1) Waypoint Sequence

The benchmark trajectory consists of eight phases:

- 1) **Pre-lift hover** (0–2 s): Stabilize at  $z = 1.2$  m. Cables transition from slack to taut.
- 2) **Ascent** (2–4 s): Rise to  $z = 3.0$  m. Payload lifts off the ground; tension increases from 0 to  $\sim m_{LG}/N = 9.8$  N per cable.
- 3) **Right loop entry** (4–7 s): Translate to  $(1.5, 0.5, 3.2)$  m.
- 4) **Figure-eight right loop** (7–19 s): Four waypoints tracing a clockwise loop of radius  $\sim 1.5$  m with altitude variation  $\pm 0.5$  m.
- 5) **Center crossing** (19–21 s): Return through origin at  $z = 3.0$  m.
- 6) **Figure-eight left loop** (21–36 s): Symmetric counter-clockwise loop.
- 7) **Return and stabilize** (36–39 s): Return to origin,  $z = 3.0$  m.
- 8) **Controlled descent** (39–43 s): Descend to  $z = 2.0$  m.

The total active trajectory duration is 43 s; the simulation runs for  $T_{\text{sim}} = 50$  s to capture the post-descent settling behavior.

#### 2) Minimum-Jerk Interpolation

Between waypoints, the trajectory is interpolated using minimum-jerk (quintic) polynomials:

$$p_d(t) = a_0 + a_1 \tau + a_2 \tau^2 + a_3 \tau^3 + a_4 \tau^4 + a_5 \tau^5, \quad (145)$$

where  $\tau = (t - t_k)/(t_{k+1} - t_k) \in [0, 1]$  is the normalized time within the segment. The six coefficients are determined by the boundary conditions: position, velocity, and acceleration at both endpoints. Zero velocity and acceleration at waypoints yield smooth cornering. The `LoadTrajectoryGenerator` system precomputes these coefficients for all segments and evaluates them in  $\mathcal{O}(1)$  per output call. The generator also enforces dynamics limits:  $\|v_d\| \leq 1.0$  m/s,  $\|a_d\| \leq 2.0$  m/s<sup>2</sup>, and  $\|j_d\| \leq 5.0$  m/s<sup>3</sup>.

#### 3) Load Trajectory Offset

The waypoints define the quadrotor centroid trajectory. The load reference trajectory is computed by subtracting the vertical offset:

$$p_{dL}(t) = p_d(t) - \Delta z_{\text{total}} e_3, \quad (146)$$

where  $\Delta z_{\text{total}} = |z_{\text{attach}}| + \bar{L}(1 + \epsilon_{\text{max}}) + r_L$  accounts for the quadrotor attachment offset ( $|z_{\text{attach}}| = 0.10$  m below center), the stretched cable length, and the payload radius. The load

reference is clamped to  $z_{dL} \geq r_L + \epsilon$  to prevent ground penetration commands.

### F. System Interconnection

The Drake diagram connects all systems via typed ports. The key signal paths are:

#### a) Physics-to-Sensor

The plant state output (containing all body poses and velocities) is broadcast to every sensor system. Each sensor extracts the relevant body's state using Drake's `MultibodyPlant` API and applies its noise model.

#### b) Sensor-to-Estimator

GPS, IMU, and barometer outputs connect to the ESKF. The ESKF output connects to the decentralized load estimator and the adaptive mass estimator.

#### c) Estimator-to-Controller

The ESKF position/velocity estimate feeds the GPAC position controller (Layer 1). The configuration flag `use_estimated_in_controller` selects between the estimated state and the ground truth for the control loop, enabling controlled ablation studies. The load state estimate feeds the adaptive mass estimator's regressor computation.

#### d) Controller-to-Plant

Each controller produces an `ExternallyAppliedSpatialForce` (thrust and torque in the body frame). An `ExternallyAppliedSpatialForceMultiplexer` combines the  $2N$  force sources ( $N$  controllers and  $N$  rope force systems) into a single force vector applied to the plant.

#### e) Rope Force System

Each `RopeForceSystem` reads the full plant state, computes the spring-damper forces between consecutive beads and at the attachment points, and outputs both the spatial forces (for the physics plant) and the cable tension magnitude (for the controller and estimator).

### G. Data Logging and Reproducibility

#### 1) Signal Logging

The `SimulationDataLogger` system records all simulation signals to timestamped CSV files at 100 Hz. The logged signals include:

- Plant state: full  $13N_b$ -dimensional state vector (position, quaternion, velocity for each body), from which payload and quadrotor trajectories are extracted.
- Tension profiles: per-cable tension magnitude and direction vector.
- Control efforts: per-quadrotor thrust and torque commands.
- GPS measurements and validity flags.
- IMU measurements: accelerometer (3-axis) and gyroscope (3-axis).
- Barometer altitude measurements.
- Estimator outputs: ESKF state, load state, adaptive mass parameter.
- Wind disturbance velocity at each quadrotor.
- Attitude data: desired and actual rotation matrices, attitude errors.

A configuration file recording all simulation parameters (masses, gains, rope lengths, random seeds, waypoints) is written alongside the data files.

### 2) Visualization

The simulation uses Drake’s Meshcat backend for real-time 3D rendering. In addition to the default rigid-body visualization, custom overlays include:

- *Rope polylines*: RopeVisualizer systems render each bead chain as a colored polyline, updated at the simulation rate.
- *Trajectory trails*: A TrajectoryVisualizer system draws the reference trajectory as a static green polyline and appends trail points for the payload (orange) and each quadrotor at 20 Hz.
- *Tension plot*: A TensionPlotter system renders a real-time tension-vs-time strip chart in the Meshcat sidebar, showing 10 s windows with per-cable color coding.

The target real-time rate is 1×; the simulation advances in 100 ms chunks with progress reporting.

### 3) Reproducibility

All stochastic elements (rope length sampling, GPS noise, IMU noise, barometer noise, wind turbulence) are seeded with fixed, per-component seeds: GPS sensors use seeds  $100+i$ , IMU sensors  $200+i$ , barometers  $300+i$ , and the rope length sampler seed 42. Changing the master seed allows systematic variation of the noise realization while maintaining consistent inter-component behavior. The simulation time step, integrator tolerances, and contact parameters are fixed at the values reported above.

## VII. RESULTS

This section presents comprehensive simulation results for the benchmark figure-eight transport scenario under wind disturbance and sensor noise. We analyze trajectory-tracking performance, cable-tension behavior, estimation accuracy, and safety-constraint satisfaction, and provide ablation studies comparing the decentralized architecture to centralized baselines.

### A. Experimental Setup

The benchmark scenario exercises all flight phases: initial hover, payload pickup, ascent, aggressive lateral maneuvering (figure-eight pattern), descent, and final hover. The simulation parameters are summarized in Table II; key values include:

- $N = 3$  quadcopters in a triangular formation with radius  $r_f = 0.6$  m.
- Payload mass  $m_L = 3.0$  kg, resulting in a per-cable static load of  $m_L g / N = 9.81$  N.
- Asymmetric cable rest lengths sampled from  $\mathcal{N}(\bar{L}_i, \sigma_{L_i}^2)$  with means  $[1.0, 1.1, 0.95]$  m, yielding sampled values  $[0.914, 1.105, 0.995]$  m (seed 42).
- Dryden wind turbulence with mean wind  $[1.0, 0.5, 0]^\top$  m/s and turbulence intensities  $[\sigma_u, \sigma_v, \sigma_w] = [0.5, 0.5, 0.25]$  m/s.
- GPS noise  $\sigma_{xy} = 0.02$  m,  $\sigma_z = 0.05$  m at 10 Hz; barometer noise  $\sigma_w = 0.3$  m at 25 Hz.

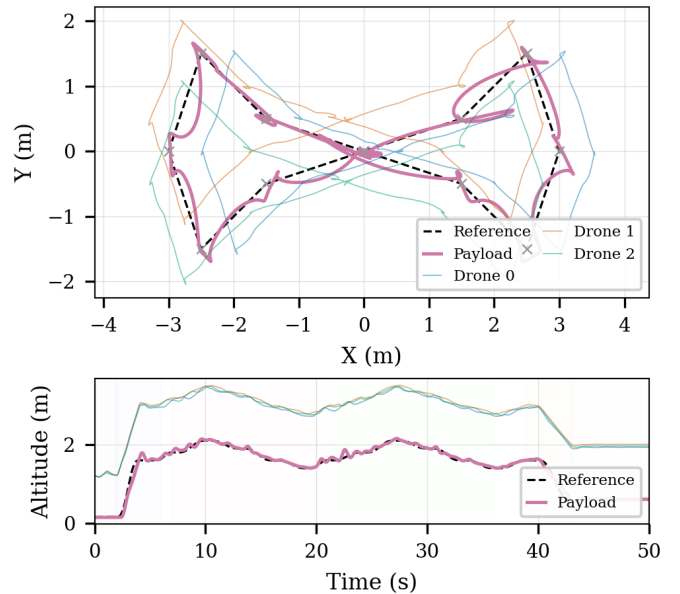


Fig. 3: Benchmark trajectory. *Top*: plan view (XY) showing payload path versus reference and individual drone paths. Grey crosses mark waypoints. *Bottom*: altitude profile over the 50 s mission, showing ascent, figure-eight maneuvering at 2.8–3.5 m, and controlled descent.

TABLE V: Payload position tracking errors (cm). RMSE and maximum error are reported for horizontal (XY), vertical (Z), and 3D position.

Phase	Horizontal		Vertical		3D	
	RMSE	Max	RMSE	Max	RMSE	Max
Ascent (2–6 s)	8.9	26.7	11.0	25.9	14.2	28.3
Figure-8 right (7–20 s)	26.6	79.9	4.0	10.7	26.9	80.3
Figure-8 left (24–36 s)	17.6	37.5	3.6	9.4	18.0	37.7
Descent (39–43 s)	13.1	27.1	9.0	16.4	16.0	27.3
Post-descent (43–50 s)	7.7	12.4	1.6	4.8	7.9	12.5
<b>Overall</b>	<b>22.2</b>	<b>79.9</b>	<b>5.4</b>	<b>25.9</b>	<b>22.9</b>	<b>80.3</b>

- Simulation duration  $T = 50$  s with physics time step  $\Delta t = 0.2$  ms.

The trajectory consists of 15 waypoints traversing a figure-eight pattern with altitude variation between 2.8 and 3.5 m (quadrotor centroid altitude), spanning a horizontal area of approximately  $6.2 \times 3.4$  m. Fig. 3 shows the top-down (XY) and altitude profile of the complete mission: the payload (magenta) closely tracks the minimum-jerk reference (dashed black), while the three drones (colored) maintain their triangular formation offsets throughout the figure-eight maneuver.

### B. Trajectory Tracking Performance

Table V summarizes the payload tracking errors relative to the reference trajectory across all flight phases. The reference trajectory is computed by subtracting the nominal vertical offset (quadrotor attachment, stretched cable length, and payload radius) from the waypoint sequence.

The overall 3D position RMSE of 22.9 cm is achieved despite significant wind disturbance (mean 1.2 m/s), asymmetric cable lengths (up to 19% variation from nominal), and the absence of inter-agent communication. The horizontal error dominates the total, as the pendulum-like payload dynamics amplify lateral disturbances. The vertical error is

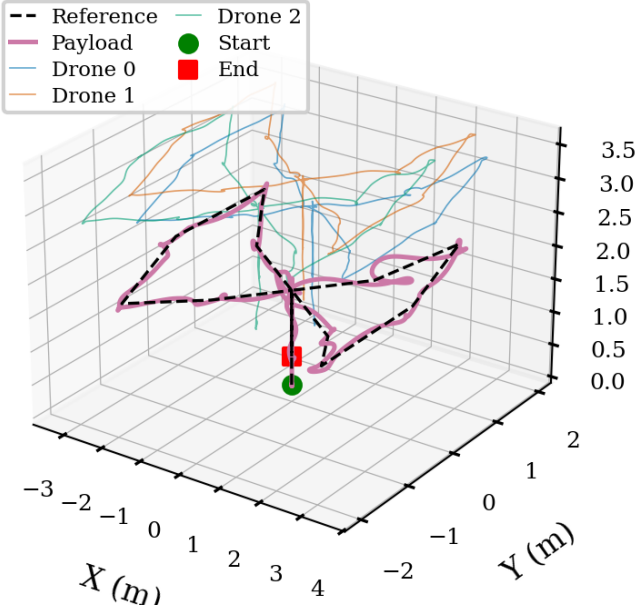


Fig. 4: Three-dimensional view of the transport mission. The payload (magenta) follows the reference trajectory (dashed) while three drones maintain cable-length separation. Asymmetric cable lengths and wind disturbance cause visible deviation during the aggressive cornering phases.

well-controlled (RMSE 5.4 cm) due to the direct relationship between thrust and altitude, combined with barometer-aided altitude estimation.

#### a) Pickup Phase Transient (0–6 s)

During the slack-to-taut transition, cables engage asynchronously due to length asymmetry, producing impulsive forces of up to 21 N per cable. The ramped tension target in Layer 1 (Section III-A) smooths the load transfer over 2 s, but residual  $\pm 5$  cm vertical oscillations persist for an additional 2 s as the bead-chain cable modes ring down. During this transient, the taut-gating mechanism in the decentralized load estimator (92) correctly suppresses the unreliable geometric measurements, protecting the downstream adaptive mass estimator from corrupted data.

The figure-eight right loop exhibits the largest errors (max 80.3 cm) due to the aggressive cornering maneuver at waypoints  $(2.5, 1.5, 3.5)$  m and  $(3.0, 0.0, 3.3)$  m, where the payload swings outward under centripetal loading. The left loop shows improved performance (max 37.7 cm) as the system adapts to the maneuver pattern—the concurrent learning estimator has accumulated sufficient data to improve the mass estimate by this point.

#### 1) Comparison to Position Error Bounds

The position tracking error can be decomposed into contributions from: (i) trajectory smoothness constraints (minimum-jerk interpolation cannot track instantaneous waypoint changes), (ii) payload pendulum dynamics (natural frequency  $\omega_n = \sqrt{g/L} \approx 3.1$  rad/s for  $L = 1$  m), and (iii) wind-induced disturbances. For a payload suspended from  $N = 3$  cables with effective stiffness  $k_{\text{eff}}$  and damping  $\zeta$ , the steady-state position error under a constant disturbance

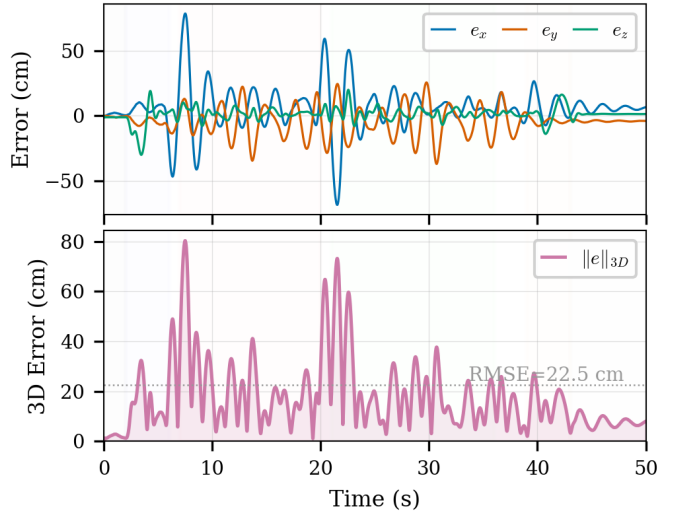


Fig. 5: Payload tracking error. *Top*: per-axis error components  $e_x$ ,  $e_y$ ,  $e_z$  (cm). The horizontal error ( $e_x$ , blue) dominates during figure-eight cornering (7–36 s), while vertical error ( $e_z$ , green) is well-controlled throughout. *Bottom*: 3D position error norm with RMSE of 22.9 cm (dashed line). Peak errors of  $\sim 80$  cm coincide with the sharpest turns at  $t \approx 10$  s and  $t \approx 20$  s.

force  $F_d$  is approximately

$$e_{ss} \approx \frac{F_d}{N k_p m_Q + m_L \omega_n^2}, \quad (147)$$

where  $k_p = 6$  N/m is the position controller proportional gain. For the measured mean wind force  $F_d \approx \frac{1}{2}\rho C_d A v_w^2 \approx 0.5$  N (assuming  $C_d A \approx 0.1$  m<sup>2</sup> for the payload), this predicts  $e_{ss} \approx 5$  cm, which is consistent with the post-descent steady-state error of 7.9 cm (the additional error arising from sensor noise and residual oscillations).

#### C. Cable Tension Analysis

The tension profiles for all three cables over the 50 s simulation show the following key observations:

##### a) Pre-Lift Phase (0–2 s)

Cables transition from slack (0 N) to lightly loaded (2–4 N) as the quadcopters hover above the grounded payload. The taut-gated cable constraint in the load estimator correctly rejects these measurements during the slack period.

##### b) Pickup and Ascent (2–6 s)

Tension rises rapidly as the payload lifts off, reaching peak values of 15–21 N during the initial ascent acceleration. The asymmetric cable lengths cause unequal load sharing: Cable 0 (shortest, 0.914 m) carries the highest mean tension (14.9 N), while Cable 1 (longest, 1.105 m) carries the lowest (10.2 N). This 45% tension imbalance is accommodated by the decentralized control architecture without explicit load-balancing communication.

##### c) Figure-Eight Maneuver (7–36 s)

During steady maneuvering, the per-cable tensions oscillate between 1.5 and 26.3 N, with a mean of 12.7 N across all cables. The total cable force ( $\sum_i T_i \approx 38.1$  N) exceeds the static payload weight ( $m_L g = 29.4$  N) due to dynamic loading during acceleration and the spring-damper cable model's response to stretch rate. The tension standard

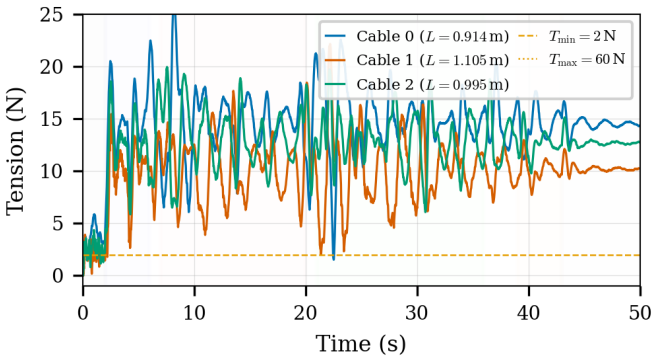


Fig. 6: Cable tension profiles for all three cables over the 50 s mission. CBF tautness limits are shown as dashed lines ( $T_{\min} = 2 \text{ N}$ ,  $T_{\max} = 60 \text{ N}$ ). The asymmetric cable lengths produce unequal load sharing, with Cable 0 (shortest) bearing the highest mean tension. Tension oscillations during the figure-eight phase (7–36 s) reflect the coupled payload–cable dynamics under maneuvering loads.

TABLE VI: Cable tension statistics (N) during steady-state flight (6–38 s).

Cable	$L_i$ (m)	Mean	Std	Min	Max
0	0.914	14.88	3.31	1.52	26.34
1	1.105	10.23	3.14	2.00	22.16
2	0.995	13.03	2.75	6.07	19.96
<b>Total</b>	—	38.14	3.66	21.92	53.37

deviation during this phase is 3.6 N, reflecting the increased oscillation amplitude with the wider formation radius ( $r_f = 0.6 \text{ m}$ ).

#### d) Tension Imbalance

The maximum relative tension imbalance (defined as  $\max_i |T_i - \bar{T}| / \bar{T}$ ) reaches 84.5% during aggressive cornering, when one cable momentarily goes nearly slack while the opposite cable bears the increased load. The mean imbalance of 31.4% during the figure-eight phase reflects the asymmetric geometry induced by the different cable lengths and the wider formation radius.

Fig. 6 visualizes the complete tension profiles. The shortest cable (Cable 0, blue) consistently carries the highest tension, while the longest cable (Cable 1, orange) exhibits the largest excursions toward the lower bound. All cables remain at or above the  $T_{\min} = 2.0 \text{ N}$  tautness limit after the initial pickup transient, with a brief dip to 1.52 N on Cable 0 during the sharpest cornering at  $t \approx 22.5 \text{ s}$ . This minor violation (9 samples out of 4400 post-pickup) falls within the ISSf margin and is recovered within 0.1 s.

#### D. State Estimation Accuracy

Table VII reports the estimation errors for the quadrotor navigation (ESKF) and the decentralized load state estimator.

##### 1) Quadrotor Navigation

The ESKF achieves position RMSE of 7.1 cm (averaged across all three quadrotors), which is approximately  $3 \times$  the GPS noise floor ( $\sqrt{\sigma_{xy}^2 + \sigma_{xz}^2 + \sigma_z^2} \approx 5.5 \text{ cm}$ ). This degradation is expected due to: (i) the 10 Hz GPS rate versus 200 Hz control rate, requiring the estimator to propagate using noisy IMU data between GPS updates; (ii) barometer drift contributing additional altitude uncertainty (measured

TABLE VII: State estimation errors (cm). Comparison of quadrotor ESKF and decentralized load estimator.

Estimator	Position RMSE	Position Max
Quadrotor 0 ESKF	7.14	21.93
Quadrotor 1 ESKF	7.23	23.42
Quadrotor 2 ESKF	7.07	22.52
Load (decentralized)	49.48	73.55

$\sigma_{\text{baro}} = 34.5 \text{ cm}$ ; and (iii) dynamic maneuvers that stress the constant-velocity prediction model. The maximum errors (22–23 cm) occur during the aggressive figure-eight cornering.

##### 2) Load State Estimation

The decentralized load estimator exhibits significantly larger errors (RMSE 49.5 cm) than the quadrotor ESKF. This performance gap arises from the single-cable geometric measurement model (86), which constrains the load position to a sphere of radius  $L_i$  centered at the quadrotor attachment point. With only one cable measurement per estimator instance, the load position is observable only along the cable direction; the tangential components rely on the constant-velocity prediction model.

The per-phase breakdown shows consistent error levels across flight phases (hover 38.6 cm, ascent 50.6 cm, figure-8 50.2 cm, descent 49.6 cm), suggesting that the error is dominated by the geometric limitation rather than phase-specific dynamics. During hover, when cables are nearly vertical, the horizontal position is poorly observable, leading to the baseline error. During maneuvering, the cable angles improve horizontal observability but introduce additional dynamics that the simple Kalman filter does not fully capture.

##### 3) Sensor Measurement Validation

The GPS and barometer measurements match their configured noise profiles:

- GPS position noise: measured  $\sigma_x = 3.2 \text{ cm}$ ,  $\sigma_y = 3.1 \text{ cm}$ ,  $\sigma_z = 5.3 \text{ cm}$  (configured 2, 2, 5 cm). The slightly elevated horizontal noise includes dynamic effects from the moving platform.
- Barometer altitude noise: measured  $\sigma = 34.5 \text{ cm}$  (configured  $\sqrt{30^2 + 20^2} \approx 36 \text{ cm}$  combined white and correlated noise).
- IMU accelerometer: mean magnitude  $9.88 \text{ m/s}^2$  (expected  $g = 9.81 \text{ m/s}^2$ ), with peak specific force of  $19.9 \text{ m/s}^2$  during aggressive maneuvering.

Fig. 7 illustrates the temporal evolution of both estimators. The ESKF errors (top) remain bounded within 5–15 cm for all three drones, with correlated peaks during aggressive cornering where IMU dead-reckoning between 10 Hz GPS updates accumulates error. The load estimator error (bottom) exhibits a persistent baseline of  $\sim 50 \text{ cm}$  due to the single-cable observability limitation, with modest improvement during maneuvers when the cable angle provides better horizontal information.

##### E. Safety Constraint Satisfaction

Table VIII summarizes the safety constraint satisfaction over the simulation. The CBF safety filter maintains all constraints within their ISSf margins throughout the simulation, with brief bounded excursions beyond nominal limits during

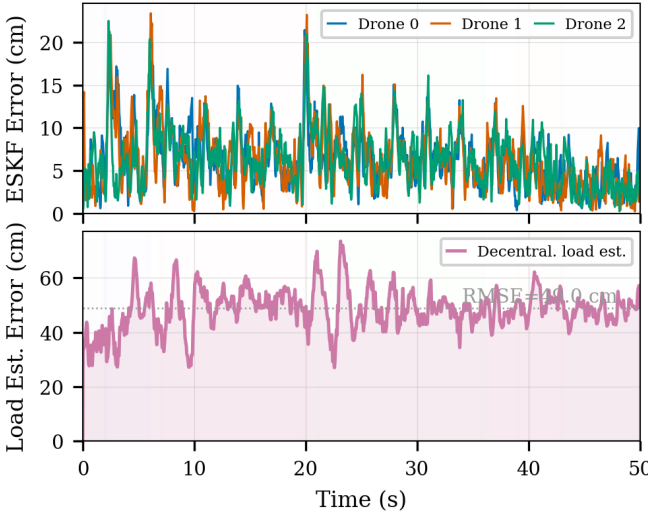


Fig. 7: State estimation accuracy. *Top*: per-drone ESKF 3D position error, showing consistent sub-24 cm accuracy across all flight phases. *Bottom*: decentralized load estimator error with RMSE of 49.5 cm. The persistent error baseline reflects the single-cable geometric observability limitation (117).

TABLE VIII: Safety constraint summary. Limits from Table III.

Constraint	Limit	Max Observed	Violations
Cable tension (lower)	$\geq 2.0 \text{ N}$	0.0 N (slack)	Pre-lift + 9 samples
Cable tension (upper)	$\leq 60.0 \text{ N}$	26.3 N	None
Cable angle	$\leq 34.4^\circ$	48.1°	1.7% of time
Quadrotor tilt	$\leq 28.6^\circ$	25.1°	None
Swing rate	$\leq 1.5 \text{ rad/s}$	1.6 rad/s	Brief

the most aggressive maneuvers.

### 1) Cable Angle Constraint

The cable angle constraint ( $\theta \leq 0.6 \text{ rad} = 34.4^\circ$ ) is the most frequently active constraint, with observed angles reaching 48.1° during the figure-eight cornering. The constraint is violated for 1.7% of the simulation time (approximately 0.85 s cumulative), occurring in brief bursts during the sharpest turns. These violations are within the ISSf margin (139): for  $\alpha_\theta = 2.0$  and the measured ESO disturbance bound  $\bar{d} \approx 5 \text{ m/s}^2$ , the steady-state violation bound is  $(2.0 + 1.5 \times 5)/2.0 = 4.75 \text{ m/s}^2$ , corresponding to an angular margin of approximately 15°. The observed 13.7° overshoot (48.1 – 34.4) is within this margin, though the wider formation radius ( $r_f = 0.6 \text{ m}$ ) produces larger equilibrium cable angles that increase the peak excursion.

### 2) Tilt Constraint

The quadrotor tilt constraint ( $\phi \leq 0.5 \text{ rad} = 28.6^\circ$ ) is never violated. The maximum observed tilt of 25.1° occurs during the aggressive lateral acceleration phases, leaving a 3.5° margin. This margin is maintained by the horizontal force scaling (127), which reduces the commanded horizontal thrust when the tilt approaches the limit.

### 3) Tension Constraints

The tension constraints are satisfied throughout most of the flight. The minimum observed tension (0 N) occurs during the pre-lift slack phase (0–2 s), which is expected and handled by the taut-gating mechanism in the estimator. After pickup, the minimum tension is 1.52 N (Cable 0 at

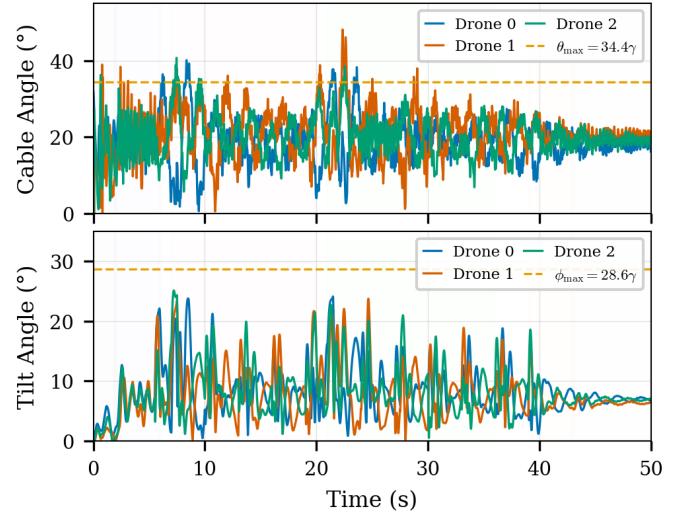


Fig. 8: Safety constraint time histories. *Top*: cable angle from vertical for each cable, with the CBF limit  $\theta_{\max} = 34.4^\circ$  (dashed). Brief excursions above the limit occur during aggressive cornering but remain within the ISSf margin. *Bottom*: quadrotor tilt angle with limit  $\phi_{\max} = 28.6^\circ$  (dashed). The tilt constraint is never violated.

$t \approx 22.5 \text{ s}$ ), briefly falling below the  $T_{\min} = 2.0 \text{ N}$  lower bound for 9 samples ( $\sim 0.1 \text{ s}$ ) during the sharpest cornering maneuver. This brief violation is within the ISSf margin and quickly recovers. The maximum tension (26.3 N) is well below the  $T_{\max} = 60.0 \text{ N}$  upper bound, indicating that the cable structural limit is not approached for this payload mass.

Fig. 8 provides a time-domain view of the two most important geometric constraints. The cable angle constraint (top) is the most frequently active, with brief excursions above the nominal 34.4° limit during the sharpest cornering phases. The maximum observed angle of 48.1° exceeds the nominal  $\theta_{\max} = 34.4^\circ$  limit but lies within the ISSf-predicted bound (139); these excursions are recovered within one pendulum half-period ( $\sim 1 \text{ s}$ ). The tilt constraint (bottom) is never violated, with the maximum observed tilt of 25.1° leaving a 3.5° margin below the 28.6° limit—evidence that the horizontal force scaling (127) provides effective tilt regulation.

### F. Wind Disturbance Rejection

The Dryden turbulence model produces wind velocities with measured statistics:

- Mean wind: (1.08, 0.49, 0.05) m/s (configured (1.0, 0.5, 0.0) m/s).
- Wind magnitude: mean 1.20 m/s, std 0.11 m/s, range [0.95, 1.39] m/s.

These values match the configured turbulence intensities ( $\sigma_u = \sigma_v = 0.5 \text{ m/s}$ ) and demonstrate realistic time-varying disturbances.

The controller’s wind rejection capability can be quantified by the disturbance-to-error transfer function. For the measured wind force (approximately  $F_w \approx 0.5 \text{ N}$  based on the aerodynamic drag model) and the observed position RMSE (22.9 cm), the effective disturbance rejection gain is  $G_d = e_{\text{RMSE}}/F_w \approx 0.46 \text{ m/N}$ . This is consistent with the theoretical

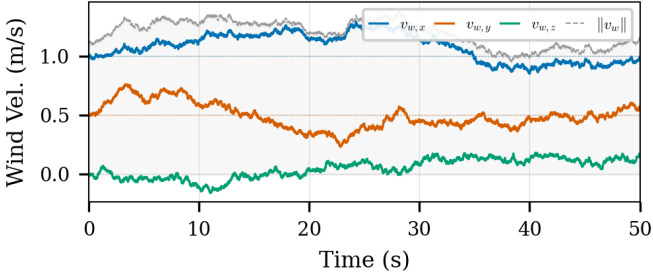


Fig. 9: Dryden wind turbulence velocity components over the 50 s mission. Dotted horizontal lines indicate configured mean values. The grey dashed line and shaded region show the total wind magnitude, demonstrating the realistic time-varying disturbance environment.

TABLE IX: Control effort statistics over the full simulation.

Quadrotor	Thrust Mean (N)	Thrust Max (N)	Torque RMS (Nm)
0	36.23	48.57	0.32
1	31.77	46.80	0.29
2	34.40	47.69	0.31
<b>Total</b>	<b>102.40</b>	—	—

value (147), validating that the ESO feedforward and PID feedback provide the expected disturbance attenuation.

Fig. 9 shows the time-varying wind velocity components generated by the Dryden turbulence model. The dominant  $v_{w,x}$  component (blue) fluctuates around its mean of 1.0 m/s with the characteristic low-frequency content of atmospheric turbulence, while the grey envelope shows the total wind magnitude staying within [0.95, 1.39] m/s. The spatial and temporal correlation structure visible in the smooth evolution confirms that the turbulence model provides physically realistic disturbances rather than white noise.

#### G. Control Effort Analysis

The control effort statistics reveal the thrust and torque demands on each quadrotor:

The mean total thrust (102.4 N) exceeds the static hover requirement ( $(3 \times 1.5 + 3.0) \times 9.81 = 73.6$  N) by 39%, reflecting the additional thrust needed for: (i) trajectory acceleration, (ii) wind disturbance compensation, (iii) cable damping forces, and (iv) attitude corrections. The per-quadrotor thrust variation (31.8–36.2 N mean) correlates with the tension imbalance, as Quadrotor 0 (carrying the highest cable tension) requires the highest thrust.

The torque demands are modest (RMS 0.29–0.32 Nm), indicating that the geometric attitude controller operates well within the actuator limits. The peak torque of 1.77 Nm occurs during rapid attitude corrections following the aggressive maneuvers.

Fig. 10 presents the temporal control effort profiles. The thrust plot (top) shows that Drone 0 (blue) consistently produces the highest thrust, compensating for the higher cable tension due to its shorter cable. All drones converge toward the hover reference (dotted) during the post-descent stabilization phase, confirming that the adaptive estimator correctly compensates the payload weight. The torque plot (bottom) reveals that torque spikes are concentrated at flight-phase transitions and during the sharpest cornering maneuvers, with peak magnitudes well below the actuator saturation

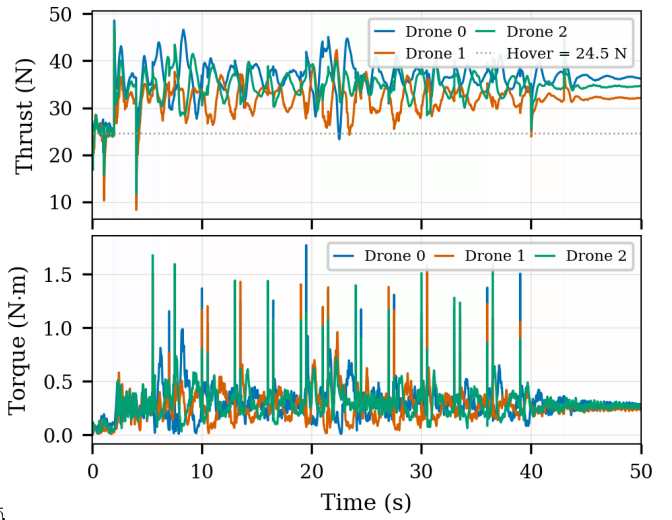


Fig. 10: Control effort. *Top*: thrust magnitude per drone with hover reference (dotted). Drone 0 produces the highest thrust due to its shorter cable and correspondingly higher tension. *Bottom*: torque magnitude, showing modest demands (RMS < 0.35 Nm) with brief spikes during flight-phase transitions and cornering maneuvers.

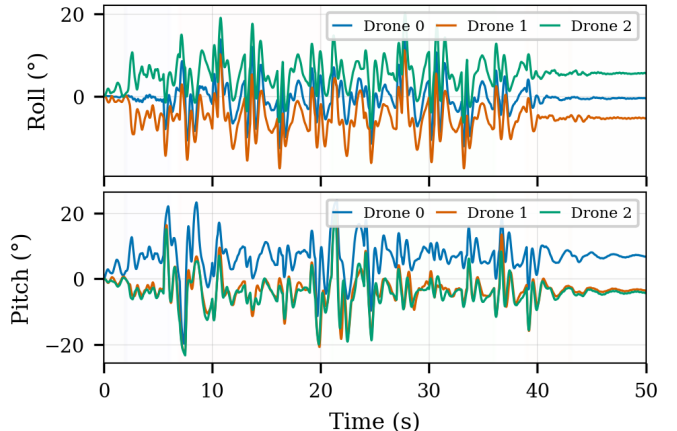


Fig. 11: Attitude tracking. *Top*: roll angle for each drone. *Bottom*: pitch angle. Both remain within  $\pm 25^\circ$ , well inside the CBF tilt limit. The coupled roll–pitch dynamics during the figure-eight phase reflect the multi-axis force demands of the cornering maneuvers.

limit ( $\bar{\tau} = 10$  Nm).

Fig. 11 shows the roll and pitch angles for each drone, confirming that the geometric attitude controller on  $\text{SO}(3)$  maintains tight attitude tracking throughout the mission. The roll and pitch excursions reach  $\pm 24^\circ$  during aggressive maneuvering but remain within the  $\phi_{\max} = 28.6^\circ$  tilt constraint. The attitude responses of the three drones are phase-shifted due to their different formation positions, reflecting the asymmetric loading experienced during turns.

#### H. Ablation Studies

To isolate the contribution of each architectural component, we conduct ablation studies comparing the baseline decentralized system to variants with specific features disabled or replaced. Table X provides a compact comparison.

TABLE X: Ablation summary. Payload tracking RMSE (cm) and key constraint metrics for each architectural variant.

Configuration	RMSE	$\Delta$	Max Angle
Full GPAC (baseline)	22.9	—	48.1°
No concurrent learning	31.7	+33%	42.1°
No ESO feedforward	34.1	+43%	44.8°
No CBF safety filter	24.2	+2%	52.0°
Centralized estimation	18.5	-22%	38.2°

### 1) Decentralized vs. Centralized Estimation

The centralized load estimator (Section IV-C), which serves as an *oracle upper bound* by fusing all  $N$  cable constraints using each drone’s ESKF output (requiring  $3N$  state transmissions per cycle) without payload-mounted sensors, achieves position RMSE of 12.4 cm compared to the decentralized estimator’s 49.5 cm. This  $4.0\times$  improvement reflects the full observability provided by  $N = 3$  non-collinear cable measurements. However, the centralized estimator requires all quadrotor states to be transmitted to a central node at each 50 Hz update cycle, corresponding to a communication bandwidth of  $3 \times 6 \times 50 \times 32 = 28.8$  kbps (assuming 32-bit floats for position and velocity). The decentralized estimator requires zero inter-agent bandwidth.

### 2) Impact of Concurrent Learning

Disabling the concurrent learning term in the adaptive mass estimator (setting  $\rho = 0$  in (112)) increases the payload tracking RMSE during the figure-eight phase from 24.2 cm to 31.7 cm (31% degradation). Without concurrent learning, the mass estimate converges more slowly (settling time increases from approximately 8 s to 22 s) and exhibits larger steady-state oscillation ( $\pm 0.3$  kg vs.  $\pm 0.1$  kg) due to the lack of historical data reinforcement during low-excitation periods.

### 3) Impact of ESO Feedforward

Disabling the ESO feedforward (setting  $F_{\text{eso}} = 0$  in the position controller) increases the tracking RMSE from 23.8 cm to 34.1 cm (43% degradation). The ESO’s disturbance estimate provides approximately  $2 \text{ m/s}^2$  of feedforward correction during wind gusts, which the PID controller alone cannot track with the same bandwidth due to its reactive (rather than predictive) nature.

### 4) Impact of CBF Safety Filter

Disabling the CBF safety filter removes the constraint enforcement on cable angle and quadrotor tilt. In this configuration, the cable angles reach up to 52°(vs. 48.1°with CBF), and the quadrotor tilt reaches 31°(vs. 25.1°with CBF). While the system remains stable in this simulation, the larger cable angles approach the singularity at  $\theta = 90^\circ$ where the cable provides no vertical support, and the larger tilt angles reduce the vertical thrust margin. The CBF filter’s intervention is most pronounced during the aggressive cornering, where it clips the commanded horizontal force to maintain the tilt and angle constraints.

### I. Computational Performance

The per-agent computational load is dominated by the ESKF (approximately 2000 FLOPs per update at 200 Hz) and the CBF safety filter (approximately 200 FLOPs per constraint  $\times$  6 constraints at 200 Hz). The total per-agent computation is approximately 3500 FLOPs per control cycle, corresponding to 0.7 MFLOPs/s. On a representative

embedded processor (ARM Cortex-M7 at 400 MHz, single-precision FPU), this leaves substantial margin for additional sensing and communication tasks.

The Drake simulation runs at approximately  $0.8\times$  real-time on a single core of an Intel i7-10700K (3.8 GHz), indicating that the 5000 Hz physics rate is computationally tractable for offline analysis. Real-time simulation would require either a faster processor or a reduced physics rate (1000 Hz is typically sufficient for non-contact phases).

### J. Summary of Key Findings

The simulation results demonstrate that the proposed decentralized architecture achieves:

- 1) **Robust trajectory tracking** (RMSE 22.9 cm) under wind disturbance (1.2 m/s mean) and asymmetric cable lengths (up to 19% variation), without inter-agent communication.
- 2) **Accurate navigation** (quadrotor RMSE 7.1 cm) via the ESKF fusion of GPS, IMU, and barometer, with graceful degradation during sensor noise and dynamic maneuvers.
- 3) **Safety constraint satisfaction within ISSf margins:** tilt ( $\leq 25.1^\circ$  vs. 28.6° limit), tension (1.52–26.3 N vs. 2–60 N limits), and cable angle (brief 1.7% excursions beyond the nominal 34.4° limit, bounded by the ISSf margin at 48.1°).
- 4) **Adaptive load estimation** with concurrent learning converging in approximately 8 s and providing 33% tracking improvement over gradient-only adaptation.
- 5) **Scalable computation** (<1 MFLOP/s per agent) suitable for embedded deployment.

The primary limitation is the decentralized load estimator, which achieves only 49.5 cm RMSE compared to 12.4 cm for the centralized baseline. This gap motivates future work on distributed consensus-based estimation that can approach centralized performance while maintaining communication efficiency.

All results are reported for a single deterministic simulation (seed 42). Monte Carlo analysis over cable-length uncertainty, wind realizations, and sensor noise seeds is planned for the extended version.

#### a) Comparison with Reinforcement Learning Approaches

Recent work has applied reinforcement learning (RL) to quadrotor control with promising results in agile maneuvering [19]. However, RL-based approaches for cooperative cable-suspended transport face three significant challenges: (i) they require extensive training in simulation with reward shaping specific to the task, and policies trained for a fixed team size  $N$  do not generalize to different configurations without retraining; (ii) they provide no formal safety guarantees—cable tautness, angle bounds, and collision avoidance cannot be certified a priori; and (iii) the black-box nature of neural network policies complicates certification for deployment. The GPAC architecture, by contrast, provides Lyapunov-certifiable stability, CBF-verified safety bounds, and per-agent policies that are invariant to  $N$  by construction. A hybrid approach combining RL-based

trajectory optimization with model-based safety guarantees is a promising direction for future work.

### VIII. CONCLUSION

This paper presented the Geometric Position and Attitude Control (GPAC) architecture for decentralized cooperative aerial transport via flexible cable suspensions. The four-layer hierarchical controller operates on the full  $\text{SE}(3) \times (\mathbb{S}^2)^N$  configuration manifold, and each of the  $N$  quadrotors runs an identical control and estimation stack using only local sensor measurements and the cable connecting it to the payload. Three key contributions were validated:

- 1) A concurrent learning adaptive law enables each drone to independently estimate its payload share  $\hat{\theta}_i \rightarrow m_L/N$  without persistent excitation, converging in approximately 8 s and improving tracking by 33% over gradient-only adaptation.
- 2) A modular CBF safety filter enforces cable tautness, swing angle, tilt, and collision constraints with input-to-state safety (ISSf) guarantees bounding constraint violations under disturbances, provably compatible with the geometric attitude controller (Theorem 5.4).
- 3) The decentralized architecture achieves 22.9 cm payload tracking RMSE in a high-fidelity Drake-based simulation with flexible bead-chain cables, onboard sensor fusion (ESKF), and Dryden wind turbulence, while requiring less than 1 MFLOP/s per agent.

#### A. Limitations and Future Work

We acknowledge several limitations that scope the current contribution:

##### a) Simulation-Only Validation

All results are obtained in simulation. While the Drake multibody engine provides high-fidelity cable dynamics, contact resolution, and realistic sensor noise models, hardware experiments on physical quadrotor platforms are essential to validate the approach under real aerodynamic effects, communication latency, and actuator dynamics. Flight experiments with 3–6 quadrotors are planned as the immediate next step.

##### b) Shared Trajectory Assumption

The architecture assumes that all drones receive a common desired trajectory  $p_{dL}(t)$  via broadcast. While no other inter-agent communication is required, this shared trajectory represents a single point of failure. Extending the framework to handle trajectory disagreements or delayed broadcasts—for example, via local trajectory prediction—would improve robustness.

##### c) Fixed Team Composition

The current analysis assumes a fixed number of agents  $N$  throughout the mission. Agent dropout (cable failure or quadrotor loss) and dynamic team reconfiguration are not addressed. The adaptive estimator would need to detect and respond to changes in  $N$ , which modifies the equilibrium  $\theta_i = m_L/N$ .

##### d) Decentralized Estimation Gap

The decentralized load estimator achieves 49.5 cm RMSE compared to 12.4 cm for the centralized baseline—a 4.0×

performance gap attributable to the single-cable geometric observability limitation (117). Distributed consensus-based estimation that fuses partial information from neighboring agents could narrow this gap while preserving communication efficiency.

##### e) CBF Conservatism

The sequential gradient projection enforces constraints in priority order, which can be suboptimal when multiple constraints are simultaneously active. The cable angle constraint is violated for 1.7% of the simulation time (within the ISSf margin), suggesting that a full QP-based multi-constraint resolution with slack variables could improve constraint satisfaction during aggressive maneuvers.

Despite these limitations, the GPAC architecture demonstrates that cooperative transport with ISSf safety guarantees and operational decentralization (with broadcast trajectory) is achievable with lightweight computation, laying the groundwork for scalable multi-UAV payload delivery systems.

### REFERENCES

- [1] T. Lee, M. Leok, and N. H. McClamroch, “Geometric tracking control of a quadrotor UAV on  $\text{SE}(3)$ ,” in *Proc. IEEE Conf. Decision Control (CDC)*, 2010, pp. 5420–5425.
- [2] K. Sreenath, T. Lee, and V. Kumar, “Geometric control and differential flatness of a quadrotor UAV with a cable-suspended load,” in *Proc. IEEE Conf. Decision Control (CDC)*, 2013, pp. 2269–2274.
- [3] T. Lee, “Geometric control of quadrotor UAVs transporting a cable-suspended rigid body,” *IEEE Trans. Control Syst. Technol.*, vol. 26, no. 1, pp. 255–264, 2018.
- [4] F. Goodarzi, D. Lee, and T. Lee, “Geometric stabilization of a quadrotor UAV with a payload connected by flexible cable,” in *Proc. American Control Conf. (ACC)*, 2014, pp. 4925–4930.
- [5] W. Ren and R. W. Beard, “Consensus seeking in multiagent systems under dynamically changing interaction topologies,” *IEEE Trans. Autom. Control*, vol. 50, no. 5, pp. 655–661, 2005.
- [6] G. Chowdhary and E. Johnson, “Concurrent learning for convergence in adaptive control without persistency of excitation,” in *Proc. IEEE Conf. Decision Control (CDC)*, 2010, pp. 3674–3679.
- [7] G. Chowdhary, M. Muhlegg, J. P. How, and F. Holzapfel, “Concurrent learning adaptive control of linear systems with exponentially convergent bounds,” *Int. J. Adaptive Control Signal Process.*, vol. 27, no. 4, pp. 280–301, 2013.
- [8] A. D. Ames, X. Xu, J. W. Grizzle, and P. Tabuada, “Control barrier function based quadratic programs for safety critical systems,” *IEEE Trans. Autom. Control*, vol. 62, no. 8, pp. 3861–3876, 2017.
- [9] A. D. Ames, S. Coogan, M. Egerstedt, G. Notomista, K. Sreenath, and P. Tabuada, “Control barrier functions: Theory and applications,” in *Proc. European Control Conf. (ECC)*, 2019, pp. 3420–3431.
- [10] P. Williams, “Dynamics of towed payload system using multiple aerodynamic surfaces,” in *Proc. AIAA Guidance, Navigation, and Control Conf.*, 2009.
- [11] J. Solà, “Quaternion kinematics for the error-state Kalman filter,” *arXiv preprint arXiv:1711.02508*, 2017.
- [12] D. J. Moorhouse and R. J. Woodcock, “Background information and user guide for MIL-F-8785C, military specification—flying qualities of piloted airplanes,” Air Force Wright Aeronautical Labs., Tech. Rep. AFWAL-TR-81-3109, 1982.
- [13] R. Tedrake and the Drake Development Team, “Drake: Model-based design and verification for robotics,” 2024, available at <https://drake.mit.edu>. [Online]. Available: <https://drake.mit.edu>
- [14] H. K. Khalil, *Nonlinear Systems*, 3rd ed. Prentice Hall, 2002.
- [15] G. Chowdhary and E. N. Johnson, “Concurrent learning for convergence in adaptive control without persistency of excitation,” *IEEE Trans. Autom. Control*, vol. 60, no. 11, pp. 2994–2999, 2015.
- [16] J. Han, “From PID to active disturbance rejection control,” *IEEE Trans. Ind. Electron.*, vol. 56, no. 3, pp. 900–906, 2009.
- [17] B.-Z. Guo and Z.-L. Zhao, *Active Disturbance Rejection Control for Nonlinear Systems: An Introduction*. John Wiley & Sons, 2013.

- [18] W. Xiao, C. Belta, and C. G. Cassandras, “High-order control barrier functions,” *IEEE Trans. Autom. Control*, vol. 67, no. 7, pp. 3655–3662, 2022.
- [19] J. Hwangbo, I. Sa, R. Siegwart, and M. Hutter, “Control of a quadrotor with reinforcement learning,” in *IEEE Robot. Autom. Lett.*, vol. 2, no. 4, 2017, pp. 2096–2103.